日本磁気学会
ISSN 1882-2924
Journal of the Magnetics Society of Japan
Electronic Journal URL: https://www.jstage.jst.go.jp/browse/msjmag

Vol.41 No.1　2017

Journal

JOURNAL OF THE MAGNETICS SOCIETY OF JAPAN

Vol.41 No.1 2017

日本磁気学会

ISSN 1882-2924

HP: http://www.magnetics.jp/ e-mail: msj@bj.wakwak.com

Electronic Journal: http://www.jstage.jst.go.jp/browse/msjmag


Physicist
Peter Grünberg
未来をどこまで想像できるか。
進みつづける時間の先に、何を見るか。
止まることのない時間の向こうに、何を思い描くか。
想像したことのない未来は、創造できない。
まっすぐな視線の先にしか、新しい常識は現れない。
先駆的なアイデアだって、革新的なテクノロジーだって、
それは、未来を自由に想像し、未来を強く渇望し、
そこに向かおうとするひたむきな意志からしか生まれない。
未来とは、前を向く者だけに与えられる、
現在という時間からのかけがえのない贈り物だ。
だから、未来に夢を見よう。未来に絵を描こう。
この世界の未来を、どこまでも想像しよう。
www.attractingtomorrow.tdk.co.jp
Attracting Tomorrow
TDK

世界初！
高温超電導型VSM

新製品

世界初*、高温超電導マグネットをVSMに採用することで
測定速度 当社従来機1/20を実現。
0.5mm cube磁石のBr, HcJ高精度測定が可能となりました。

*2014年7月 東英工業調べ

測定結果例

高温超電導VSMによるNdFeB(sint.) 0.5mm cube BHカーブ

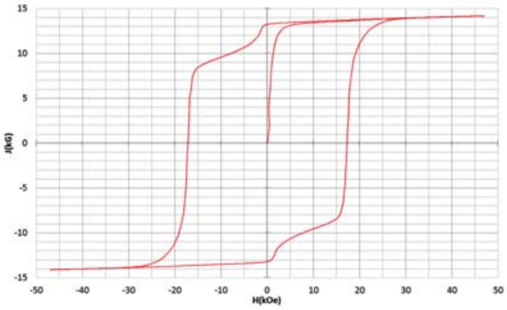

磁化測定レンジ：0.2emu
Br = 13.2kG　HcJ = 17.2kOe

高温超電導VSMによるNdFeB(sint.) 1mm cube BHカーブ

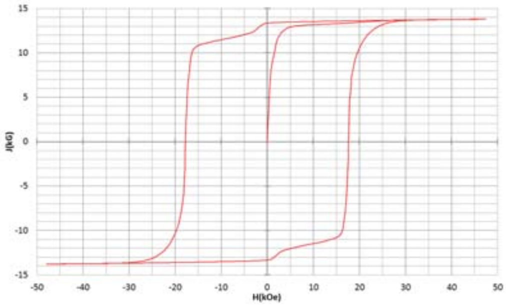

磁化測定レンジ：2emu
Br = 13.3kG　HcJ = 17.7kOe

高温超電導VSMによるNdFeB(sint.) 4mm cube BHカーブ

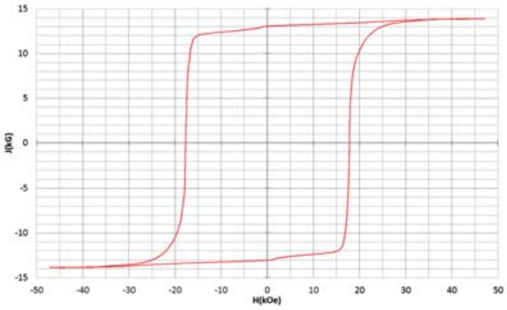

磁化測定レンジ：100emu
Br = 13.1kG　HcJ = 17.8kOe

高速測定を実現

高温超電導マグネット採用により、高速測定を実現しました。Hmax= 5Tesla, Full Loop 測定が2分で可能です。
（当社従来機：Full Loop測定 40分）

小試料のBr,HcJ高精度測定

0.5mm cube磁石のBr,HcJ高精度測定ができ、表面改質領域を切り出しBr,HcJの強度分布等、微小変化量の比較測定が可能です。
また、試料の加工劣化の比較測定が可能です。

試料温度可変測定

−50℃～+200℃温度可変UNIT（オプション）

磁界発生部の小型化

マグネットシステム部寸法：0.8m×0.3m×0.3m

TOEI 東英工業株式会社
http://www.toeikogyo.co.jp
〒194-0035 東京都町田市忠生1-8-13
TEL:042-791-1211　FAX:042-792-0490
E-mail : sales@toeikogyo.co.jp

COMSOL MULTIPHYSICS®

有限要素法解析ソフトウェア COMSOL Multiphysics®

マルチフィジックスの進化論

無制限・強連成で実現象に即したシミュレーション事例のご紹介

永久磁石を利用した磁気軸受の解析例

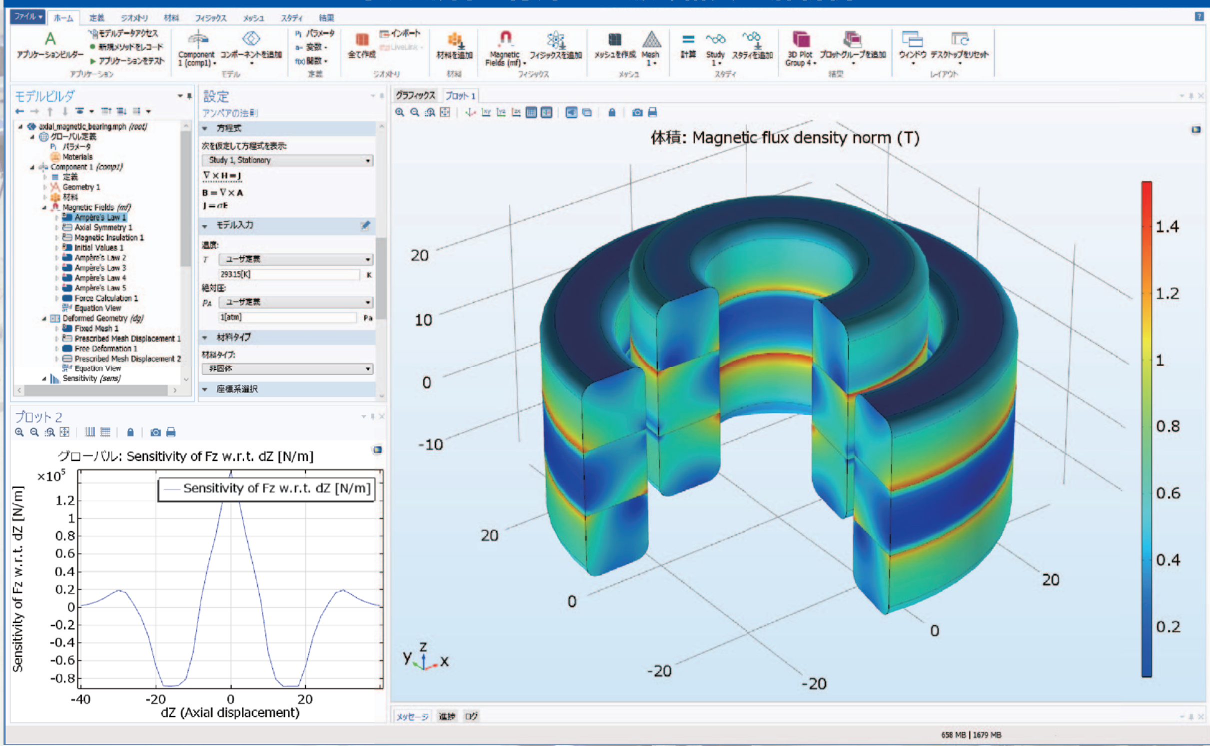

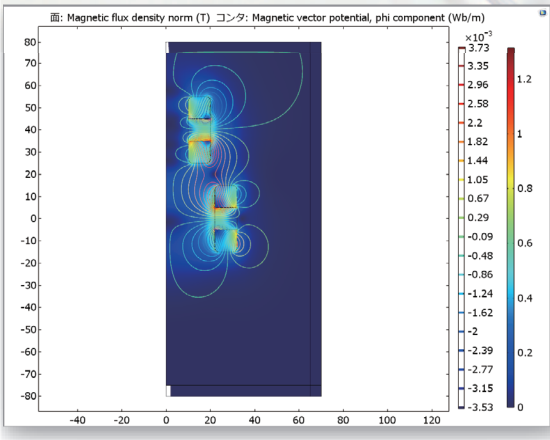

永久磁石を使用した磁気軸受

永久磁石を使用した軸受はターボ機械、ポンプ、モータ、発電機やフライホイール式エネルギー貯蔵システムなど、様々な分野で使用されています。非接触かつ潤滑不要で保守整備を大幅に省略できる点は、従来の機械式ベアリングと比べて重要なメリットです。
この例では、軸方向の永久磁石軸受の磁気力と剛性などの設計パラメータを計算する方法を示しています。
※AC/DCモジュールはCOMSOL Multiphysicsと併用するアドオン製品です。

AC/DC モジュールの適用例

- AC/DC 電流分布、電場分布
- バイオヒーティング
- コイルとソレノイド
- SPICE 回路とフィールドシミュレーション
- 接触抵抗
- 電磁両立性 (EMC) および電磁妨害 (EMI)
- 電磁力およびトルク
- 電磁力シールド
- 電気機械の変形
- ホール効果を利用したセンサ
- インシュレータ、コンデンサ、誘電体
- モータ、ジェネレータ、および他の電気機械
- 非線形材料
- 寄生容量とインダクタンス
- 永久磁石と電磁石
- 多孔質材料
- 抵抗および誘導加熱
- センサ
- 超伝導体
- 変圧器とインダクタ

COMSOL Multiphysics® なら、今まで不可能だった 3 種以上のマルチフィジックス解析を強連成で実現できます。30 日間全機能無料トライアル、無料の導入セミナー、1000種を超える世界の様々な事例をご提供いたします。詳しくは、下記の弊社営業部までお問い合せください。

COMSOL

http://www.comsol.jp

KESCO KEISOKU ENGINEERING SYSTEM
計測エンジニアリングシステム株式会社
http://www.kesco.co.jp/comsol/
Tel : 03-5282-7040 ・ Fax : 03-5282-0808

新製品　面内 / 垂直同時 Kerr ループ測定装置

局所領域の面内 / 垂直方向の磁化成分の同時測定！

※特徴

- 斜め入射 Kerr 効果を利用した面内 / 垂直方向の磁化成分の同時測定
- 逆方向入射光学系による面内成分と垂直成分の分離
- 対物レンズを使用した局所領域のヒステリシスループの測定

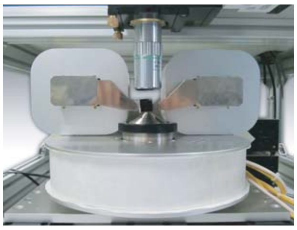

面内 / 垂直磁場発生可能な3 極電磁石

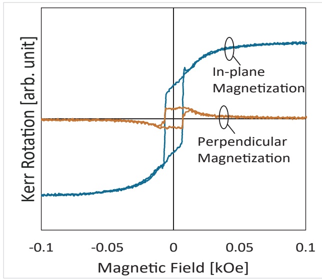

測定例

マスクレス露光装置 PALET

高速・広範囲・低価格の DMD 式マスクレス露光装置

※特徴

- 任意の画像データや CAD で作成したデータをレジストに一括露光
- 実験室でのフォトリソグラフィ作業を大幅に簡素化
- 最小線幅 3μm の露光が可能
- 約 1 秒の露光時間（弊社標準レジストにおいて）
- 自動ステージとの組み合わせで 20×20mm のエリアでの露光が可能

以上の製品以外に、 30 年の研究現場への対応経験に基づいた高精度・高性能の Kerr 効果測定装置、Faraday 効果測定装置など、 各種磁気光学製品の取り揃えがございます。
お気軽にお問合せください。

レーザとレーザ応用システム製品の総合メーカー
NEOARK ネオアーク株式会社
営 業 部 / 〒156-0041 東京都世田谷区大原2-17-6-108 TEL(03)6379-5539 FAX(03)6379-5688
大阪支店 / 〒541-0056 大阪市中央区久太郎町2-3-8-201 TEL(06)6271-5123 FAX(06)6271-5110
本社 第1工場・第2工場 / 八王子市
URL http://www.neoark.co.jp E-mail:info@neoark.co.jp

Journal of the Magnetics Society of Japan
Vol. 41, No. 1

Electronic Journal URL: https://www.jstage.jst.go.jp/browse/msjmag

CONTENTS

J. Magn. Soc. Jpn., **41**, 1-9 (2017)

<Paper>

A New Model Calculation Using Probability for Heat-Assisted Magnetic Recording

T. Kobayashi, F. Inukai, K. Enomoto, and Y. Fujiwara

Graduate School of Engineering, Mie Univ., *1577 Kurimamachiya-cho, Tsu 514-8507, Japan*

We propose a new model calculation using the reversal probability of grain magnetization for heat-assisted magnetic recording (HAMR). Our new model calculation can obtain the bit error rate as a function of the writing field H_w for a given anisotropy constant ratio K_u / K_{bulk}, which is a new parameter that we introduced. The physical implication of the recording time window proposed in the micromagnetic calculation is discussed using the new model calculation. Although the recording time window is a good guideline for write-error and erasure-after-write (EAW), EAW cannot be determined solely by the recording time window. The influence of EAW is accurately examined. The allowable range of H_w and K_u / K_{bulk} is also provided for various Curie temperatures T_c. T_c and the heat-transfer thermal gradient are important parameters for reducing K_u / K_{bulk}.

Key words: heat-assisted magnetic recording, model calculation, anisotropy constant ratio, recording time window, Curie temperature, thermal gradient

1. Introduction

Various methods have been proposed with the aim of increasing the areal density of magnetic recording beyond the trilemma limit[1)] for granular media. The methods include shingled magnetic recording (SMR), the use of media with a relatively large grain size or bit patterned media (BPM), heat-assisted magnetic recording (HAMR), and microwave-assisted magnetic recording.

It has been reported that the medium thermal stability factor $K_u V / kT$ must exceed 60 to ensure that the grain magnetization direction remains stable during 10 years of archiving, where K_u, V, k, and T are the grain anisotropy constant, the grain volume, the Boltzmann constant, and temperature, respectively. In our previous papers[2, 3)], we evaluated the statistical thermal stability factor TSF_{10} corresponding to a value of 60, that is, $K_u V / kT > \mathrm{TSF}_{10}$, and we showed that the minimum K_u value for the stability is reduced by decreasing the grain number per bit (increasing the grain size) since V increases despite the fact that TSF_{10} increases. Furthermore, we also showed that the standard deviation of the dot size for BPM must be restricted to a small value.

We have already reported a HAMR model calculation[4)] using TSF_{10} in order to shorten the calculation time and grasp the physical implications. In that paper, we introduced the anisotropy constant ratio K_u / K_{bulk} as a design guideline. K_u / K_{bulk} is the intrinsic ratio of medium K_u to bulk K_u. We must design a medium with a smaller K_u / K_{bulk} if we are to achieve good media productivity. We have subsequently improved our model calculation by introducing a statistical thermal stability factor during writing, and we revealed the dependence of the minimum K_u / K_{bulk} value on the change of one parameter among many design parameters[5)]. As a result, we found that increasing the writing temperature T_w is only effective for reducing K_u / K_{bulk}. We also provided examination results for a combination of more than two parameters[6)]. In conclusion, the combinations that can reduce K_u / K_{bulk} always have SMR as one parameter. However, the use of SMR sometimes degrades the read/write performance of the hard drive. Although a lower T_w is better in terms of the heat resistance of the writing head and/or the surface lubricant, increasing T_w appears to be the only way of reducing K_u / K_{bulk} for HAMR media. Increasing T_w has many advantages in addition to reducing K_u / K_{bulk} [7)]. We have recently improved our model calculation[8)] by introducing the concept of the recording time window[9)] proposed in a micromagnetic simulation. This improvement means the results obtained using the model calculation become consistent with those obtained using the micromagnetic simulation.

In this study, we propose a new HAMR model calculation using the reversal probability of grain magnetization for each attempt. The required statistical thermal stability factor (TSF) is a function of the bit error rate (bER). Therefore, a previous model calculation using TSF can obtain the minimum K_u / K_{bulk} value for a given bER. A new model calculation can obtain the bER as a function of the writing field H_w for a given K_u / K_{bulk}. We discuss the physical implication of the recording time window using a new model calculation. The allowable ranges of H_w and K_u / K_{bulk} are also provided for various Curie temperatures.

2. Calculation Conditions

2.1 Recording conditions

The medium was assumed to be granular. The arrangement of the grains was not considered. Figure 1 (a) is a schematic illustration of the area near the writing position for HAMR. The writing field H_w is applied to a wide area including the writing position. The circle denoted the writing temperature T_w is an isotherm of T_w, and d_w is the heat-spot diameter. T_w is defined in 3.1. The white regions indicate upward or downward magnetization, and the gray regions indicate a magnetization transition that contains upward and downward magnetization grains. The transition region spreads to adjacent tracks as a result of rewriting operations on the i th track. T_{adj} is the maximum temperature at which information in adjacent tracks can be held during rewriting. Δy is the distance between T_w and T_{adj}, and was assumed to be $d_T - d_w + D_m/2$, where d_T is the track pitch and D_m is the mean grain size. d_B is the bit pitch.

Figure 1 (b) shows the writing-head configuration. We assume that the main-pole size of the head is 600 nm (down-track direction) × 300 nm (cross-track direction), and the writing position is located on the trailing side of the main pole. H_{head} is the maximum head field that can hold information under the main pole during rewriting. The maximum temperature under the main pole is T_a, which is the maximum ambient temperature of the hard drive, and is assumed to be 330 K.

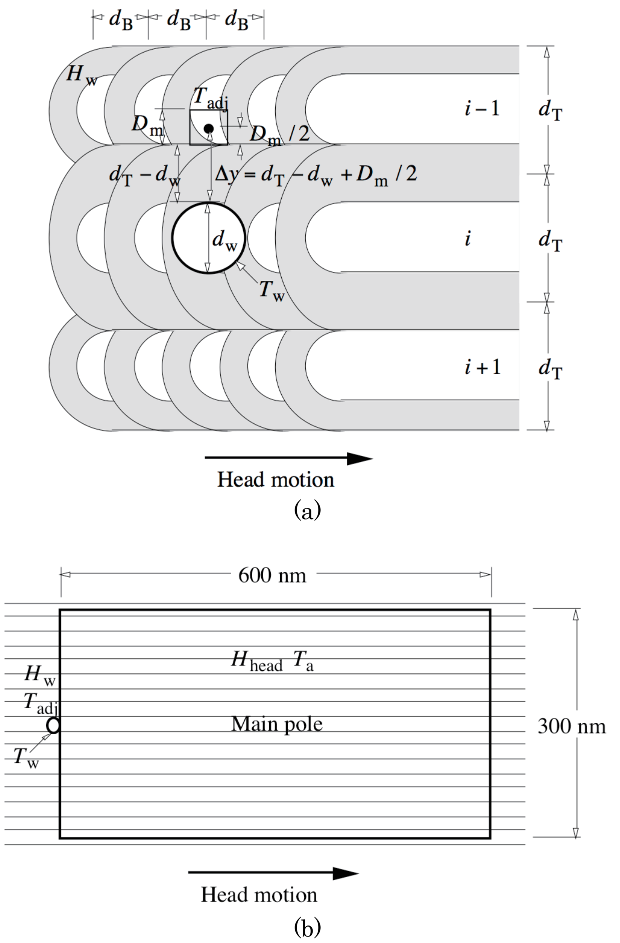

Fig. 1 Schematic illustrations of (a) writing position and (b) writing-head configuration.

Table 1 Recording parameters and standard values.

User areal density (Tbpsi)	4
Bit area $S = d_B \times d_T$ (nm^2)	140
Bit aspect ratio d_T/d_B	3
Heat-spot diameter d_w	$d_T/2$
Ambient temperature T_a (K)	330
Linear velocity v (m/s)	10

The recording parameters and the standard values are summarized in Table 1. The areal density calculated from the bit area S is 0.6 Tbpsi larger than the user areal density. The difference is the data for the error correction code and others.

$d_w = d_T/2$ is a design parameter, and is changed by the light power used for heating. If the light power alone is increased for a medium with the same Curie temperature T_c, the temperature profile increases and the written bits will be spread in the cross-track direction. Thus it becomes impossible to keep the track pitch constant. Therefore, we must adjust T_c to maintain d_w when we change the temperature profile by changing the light power.

2.2 Medium conditions

The standard medium structure is shown in Fig. 2. The standard medium consists of four layers, that is, a recording layer RL (Fe-Pt base, thickness h = 8 nm), an interlayer 1 IL1 (MgO base, 5 nm), an interlayer 2 IL2 (Cr base, 10 nm), and a heat-sink layer HSL (Cu base, 30 nm). The x, y, and z axes are the down-track, cross-track, and thickness directions, respectively. d_w is defined at the heat-spot edge and is at the center of the RL layer in the thickness direction. The two positions of T_w in Fig. 2 are at a distance of d_w in the cross-track direction as shown in Fig. 1 (a).

The medium parameters and the standard values are summarized in Table 2. D_m can be calculated from $\sqrt{S/n} - \Delta$, where n is the grain number per bit and Δ is the non-magnetic spacing between grains. K_{um} is the mean anisotropy constant. The standard deviation of the Curie temperature σ_{Tc} is assumed to be zero.

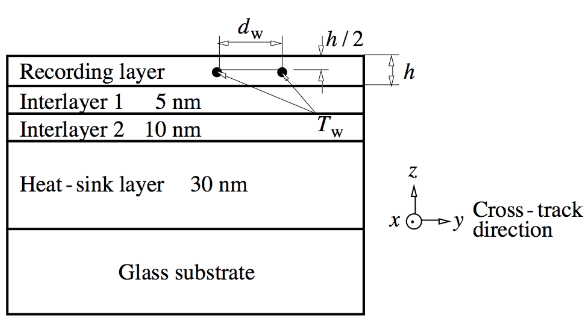

Fig. 2 Standard medium structure and definition of writing temperature T_w.

Table 2 Medium parameters and standard values.

RL thickness h (nm)	8
Non - magnetic spacing Δ (nm)	1
Grain number per bit n (grain / bit)	4
Standard deviation of grain size σ_D / D_m (%)	10
Standard deviation of anisotropy σ_K / K_{um} (%)	0
Standard deviation of Curie temp. σ_{Tc} / T_c (%)	0

The temperature dependence of the magnetization M_s was determined using a mean field analysis[4], and that of K_{um} was assumed to be proportional to M_s^2. T_c can be adjusted by the Cu simple dilution of $(Fe_{0.5}Pt_{0.5})_{1-z}Cu_z$. $M_s(T_c, T)$ is a function of T_c and T, and $M_s(T_c = 770\text{ K}, T = 300\text{ K})$ = 1000 emu/cm³ was assumed. On the other hand, $K_{um}(T_c, K_u / K_{bulk}, T)$ is a function of T_c, K_u / K_{bulk}, and T, and $K_{um}(T_c = 770\text{ K}, K_u / K_{bulk} = 1, T = 300\text{ K})$ = 70 Merg/cm³ was assumed. K_u / K_{bulk} is the intrinsic ratio of medium K_u to bulk K_u. It is necessary to design a medium with a smaller K_u / K_{bulk} in terms of achieving good media productivity.

2.3 Heat-transfer calculation conditions

The heat-transfer calculation conditions including the thermal conductivities for each layer are the same as those reported in a previous paper[4].

The heat-transfer thermal gradients $\partial T / \partial x$ for the down-track direction and $\partial T / \partial y$ for the cross-track direction are calculated by a heat-transfer simulation. $\partial T / \partial x$ and $\partial T / \partial y$ for $T_w = T_{wj}$ can be calculated using those for $T_w = T_{wi}$ as

$$\frac{\partial T}{\partial x}(T_{wj}) = \frac{\partial T}{\partial x}(T_{wi}) \frac{T_{wj} - T_a}{T_{wi} - T_a} \quad \text{and} \tag{1}$$

$$\frac{\partial T}{\partial y}(T_{wj}) = \frac{\partial T}{\partial y}(T_{wi}) \frac{T_{wj} - T_a}{T_{wi} - T_a}, \tag{2}$$

respectively. Equations (1) and (2) are valid for T_c instead of T_w since $T_w \approx T_c$. It is important that the heat-transfer thermal gradient is simultaneously increased as T_w (T_c) increases. Since $\partial T / \partial x \approx \partial T / \partial y$, $\partial T / \partial x = \partial T / \partial y$ is expressed as $\partial T / \partial x(y)$ in the following.

Table 3 Bit error rate calculation parameters and standard values.

Attempt frequency f_0 (s^{-1})	10^{11}
(Attempt period τ_{AP} (ns))	0.01
Maximum rewriting number N_{rew}	10^4
Signal threshold	0.35
Bit error rate bER	10^{-3}

2.4 Bit error rate calculation conditions

The bit error rate (bER) calculation parameters and the standard values are summarized in Table 3.

The statistical thermal stability factor TSF is calculated statistically using many bits. Each bit has n grains, and the grains have various sizes D and anisotropy constants K_u. D (lognormal distribution) and K_u (normal distribution) are randomly generated by a computer. Each grain has the grain error probability P

$$P = 1 - \exp\left(-f_0 \tau \exp\left(-\text{TSF} \cdot \left(\frac{D}{D_m}\right)^2 \cdot \frac{K_u}{K_{um}}\right)\right), \tag{3}$$

where τ is time. TSF is the thermal stability factor for $D = D_m$ and $K_u = K_{um}$, and is unrelated to K_u. The bER is a function of $P(\tau, \text{TSF})$, n, σ_D, and σ_K. If the bER is fixed, TSF is a function of τ, n, σ_D, and σ_K, that is, $\text{TSF}(\tau, n, \sigma_D, \sigma_K)$[2, 3].

Errors occur in some grains of a bit. It is assumed that if the sum of the area with no error grains ΣD_i^2 is 35 % larger than nD_m^2 in one bit, the bit has no error. The maximum allowable bER is assumed to be 10^{-3}.

3. Calculation Method

3.1 Reversal probability of grain magnetization

First, we explain the reversal probability of grain magnetization and the recording time window. The magnetization reversal number during τ is given by

$$f_0 \tau \exp(-K_\beta), \tag{4}$$

where K_β is the medium thermal stability factor. When $\tau = \tau_{AP} = 1/f_0$ = 10^{-11} s = 0.01 ns, Eq. (4) becomes

$$\exp(-K_\beta), \tag{5}$$

where τ_{AP} is the attempt period. Equation (5) is the reversal probability of grain magnetization for each attempt. For example, when K_β = 0, $\exp(-K_\beta)$ becomes one, where M_s reversal always occurs for each attempt. $K_{\beta+}$ where M_s is parallel to the writing field H_w, and $K_{\beta-}$ where M_s is antiparallel to H_w are expressed by

$$K_{\beta+}(T, H_w) = \frac{K_u(T)V}{kT}\left(1 + \frac{H_w}{H_c(T)}\right)^2, \tag{6}$$

and

$$K_{\beta-}(T, H_w) = \frac{K_u(T)V}{kT}\left(1 - \frac{H_w}{H_c(T)}\right)^2 \quad (H_w \le H_c(T)),$$

$$K_{\beta-}(T, H_w) = 0 \quad (H_c(T) < H_w), \tag{7}$$

respectively, where H_c is the coercivity. Therefore, the probability p_+ for each attempt where M_s and H_w change from parallel to antiparallel is expressed by

$$p_+ = \exp\left(-K_{\beta +}\right). \tag{8}$$

On the other hand,

$$p_- = \exp\left(-K_{\beta -}\right) \tag{9}$$

is the probability for each attempt where M_s and H_w change from antiparallel to parallel.

In this paper, the recording time window τ_{RW} is defined by

$$\tau_{RW} = \frac{T_c - T_w}{\left(\partial T / \partial x\right) \cdot v}, \tag{10}$$

where v is the linear velocity. Since $v = \partial x / \partial t$, $\left(\partial T / \partial x\right) \cdot v$ is the cooling rate $\partial T / \partial t$. Therefore, τ_{RW} is the cooling time from T_c to T_w. And then, the relationship between H_w and T_w is defined by

$$\begin{aligned} H_w &= H_{cm}(T_c, K_u / K_{bulk}, T_w) \\ &= \frac{2K_{um}(T_c, K_u / K_{bulk}, T_w)}{M_s(T_c, T_w)}, \end{aligned} \tag{11}$$

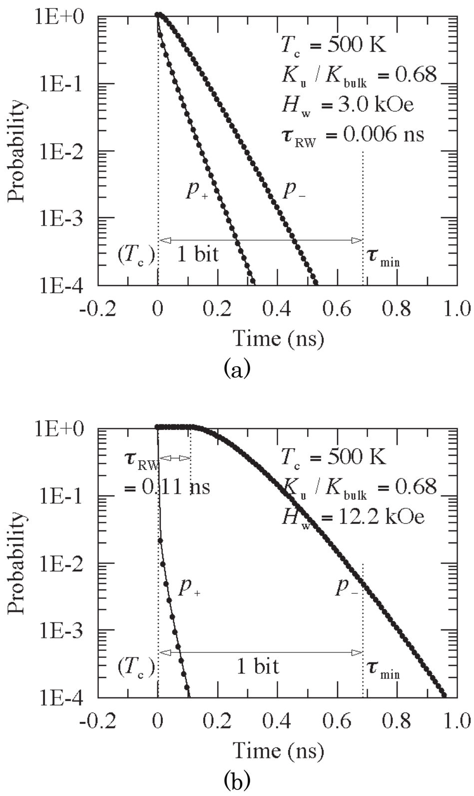

Fig. 3 Dependence of reversal probability of grain magnetization on time for (a) writing field H_w = 3.0 kOe and (b) 12.2 kOe.

where H_{cm} is the mean coercivity. The media can be designated by T_c and K_u / K_{bulk}. On the other hand, τ_{RW} is a function of T_c, K_u / K_{bulk}, $\partial T / \partial x$, v and H_w since T_w is a function of T_c, K_u / K_{bulk} and H_w.

Figure 3 shows the dependence of the reversal probability of grain magnetization on time. The time corresponding to T_c is 0 ns, and the minimum magnetization transition window $\tau_{min} = d_B / v$ corresponding to 1 bit is 0.68 ns since d_B is 6.8 nm and v is 10 m/s. The time after τ_{min} corresponds to the next bit. The filled circles are the probabilities for each attempt. The p_+ and p_- values are both one at 0 ns since $K_{\beta\pm} = 0$. p_- is always equal to one during τ_{RW}. A lower p_+ and a higher p_- are better between 0 and τ_{min} in terms of stable writing, and lower p_+ and p_- values are both better after τ_{min} in terms of information (written bit) stability.

Figure 3 (a) shows the result when T_c = 500 K, K_u / K_{bulk} = 0.68 and H_w is low (= 3.0 kOe). The resulting τ_{RW} value is 0.006 ns, and τ_{RW} is too short. p_- is rapidly decreased after 0 ns and p_+ is not sufficiently low before τ_{min}, which is not suitable for stable writing. This corresponds to write-error (WE).

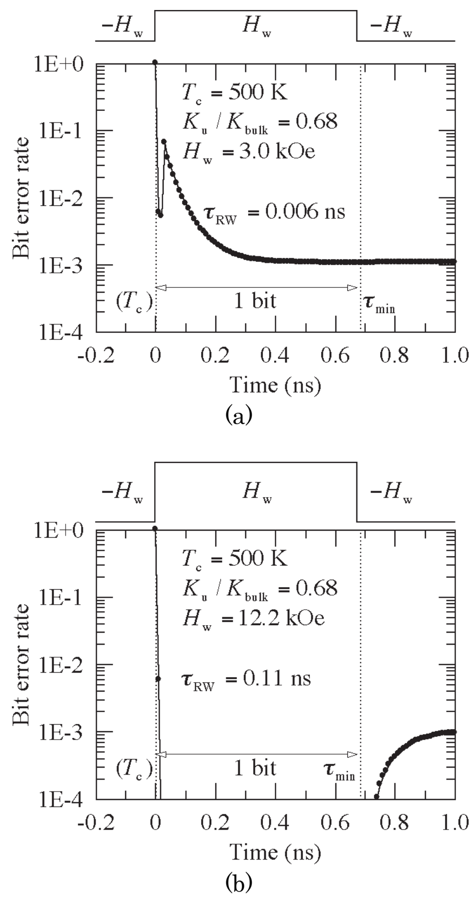

Fig. 4 Dependence of bit error rate on time for (a) writing field H_w = 3.0 kOe and (b) 12.2 kOe.

Figure 3 (b) shows the result when T_c = 500 K, K_u / K_{bulk} = 0.68 and H_w is high (= 12.2 kOe). The resulting τ_{RW} value is 0.11 ns, and τ_{RW} is too long. In this case, p_- is sufficiently high and p_+ is sufficiently low before τ_{RW}. Therefore, low WE can be expected. However, p_- has a relatively large value after τ_{min} corresponding to the next bit, which is unsuitable as regards the information stability at the next bit when the direction of H_w is changed after τ_{min}. This corresponds to erasure-after-write (EAW).

3.2 Bit error rate calculation

The bER can be calculated by the Monte Carlo method using the reversal probability of grain magnetization $p_\pm$ for each attempt period. First, the medium is determined by T_c and K_u/K_{bulk}. The grain temperature falls from T_c according to $\partial T/\partial x$ and v during the writing process. The magnetic property and then $p_\pm$ are calculated by employing a mean field analysis for each attempt period. The magnetization direction can be determined by the Monte Carlo method for each attempt period. The bER is obtained from the mean of 10^6 bits since the results are scattered.

Figure 4 (a) shows the bER dependence on time for the same conditions shown in Fig. 3 (a). The direction of H_w is changed after τ_{min} to examine the EAW. The bER remains high before τ_{min} since H_w is too low, that is, WE. A case where H_w is too high is shown in Fig. 4 (b), which corresponds to Fig. 3 (b). Although the bER is sufficiently low before τ_{min}, it increases after τ_{min}, that is, EAW.

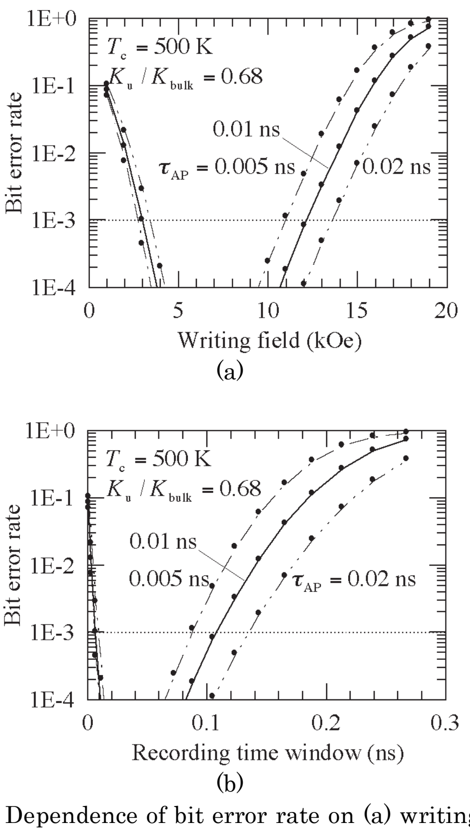

Fig. 5 Dependence of bit error rate on (a) writing field and (b) recording time window for various attempt periods τ_{AP}.

3.3 Attempt period

The attempt period is an uncertain parameter. Figure 5 shows the bER dependence on (a) H_w and (b) τ_{RW} for various attempt periods τ_{AP}. A high bER in a low H_w (a short τ_{RW}) range is caused by WE, and that in a high H_w (a long τ_{RW}) range is caused by EAW. The overall tendencies of bER are not greatly changed by doubling τ_{AP}.

3.4 HAMR conditions

Five HAMR conditions are examined to estimate the allowable ranges of H_w and K_u/K_{bulk}.

Condition I is the information stability during 10 years of archiving. The minimum K_u/K_{bulk} value can be calculated using a previous model calculation[4] by solving

$$\frac{K_{um}(T_c,\ K_u/K_{bulk},\ T_a)V_m}{kT_a} = \mathrm{TSF}_{10} \equiv \mathrm{TSF}(10\ \text{years},\ n,\ \sigma_D,\ \sigma_K), \tag{12}$$

where V_m is the grain volume for mean grain size.

Condition II is the restriction of WE. The minimum H_w value for WE can be calculated using the new model calculation mentioned in **3.2**.

Condition III is the restriction of EAW. The maximum H_w value for EAW can also be calculated using the new model calculation mentioned in **3.2**.

Condition IV is the information stability in adjacent tracks during rewriting, that is, adjacent-track-interference (ATI). The maximum H_w value for ATI can be calculated by solving

$$K_{\beta\_}(T_{adj},\ H_w) = \mathrm{TSF}_{adj} \equiv \mathrm{TSF}\left(\frac{d_B}{v}\times N_{rew},\ n,\ \sigma_D,\ \sigma_K\right) \tag{13}$$

(thermal stability condition)[5],

$$\frac{T_w(H_w)-T_{adj}}{\Delta y} = \frac{\partial T}{\partial y} \tag{14}$$

(thermal gradient condition)[5], and Eq. (11).

Condition V is the information stability under the main pole during rewriting. The maximum H_{head} value can be calculated using a previous model calculation[5] by

$$H_{head} = H_{cm}(T_a)\left(1-\sqrt{\frac{\mathrm{TSF}_{head}}{K_{um}(T_a)V_m/(kT_a)}}\right), \tag{15}$$

where

$$\mathrm{TSF}_{head} \equiv \mathrm{TSF}(\tau_{head}\times N_{rew}\times(N_T-1),\ n,\ \sigma_D,\ \sigma_K), \tag{16}$$

$\tau_{head} = 600\ \mathrm{nm}/v$, and $N_T = 300\ \mathrm{nm}/d_T$.

4. Calculation Results

4.1 Heat-transfer thermal gradient

τ_{RW} is a function of T_c, K_u/K_{bulk}, $\partial T/\partial x$, v and H_w. First, we examine the relationship between τ_{RW} and $\partial T/\partial x$. Figure 6 shows the dependence of bER on (a) H_w and (b) τ_{RW} for various $\partial T/\partial x$ values. Open circles indicate the bER for EAW when τ_{RW} = 0.1 ns. As shown in Fig. 6 (b), although the bER values for WE in a short τ_{RW} range (< 0.02 ns) are almost the same for various $\partial T/\partial x$ values, the bER for EAW at τ_{RW} = 0.1 ns for $\partial T/\partial x$ = 4.9 K/nm is higher than that for 6.9 K/nm.

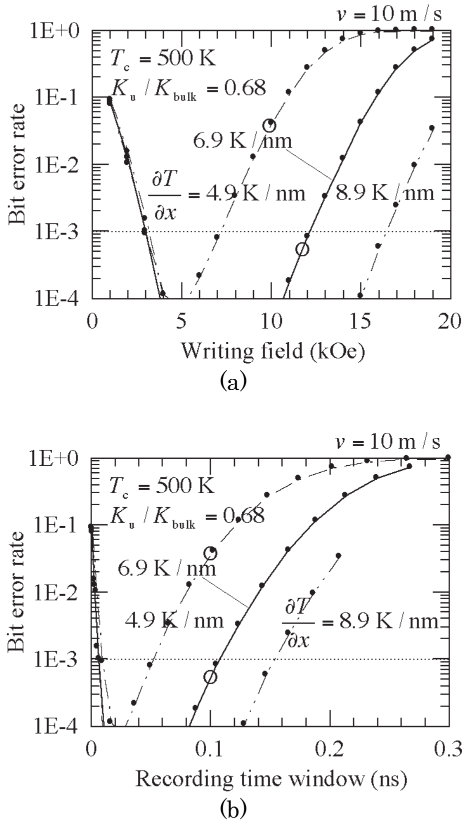

Fig. 6 Dependence of bit error rate on (a) writing field and (b) recording time window for various heat-transfer thermal gradients $\partial T/\partial x$.

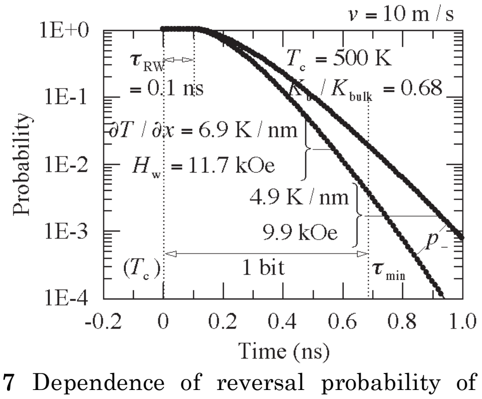

Fig. 7 Dependence of reversal probability of grain magnetization on time for heat-transfer thermal gradients $\partial T/\partial x$ = 4.9 K/nm and 8.9 K/nm.

This difference can be explained using Fig. 7. The bER for EAW is determined by p_- after τ_{min}. Although the τ_{RW} values are the same, the p_- values after τ_{min} are different since the $\partial T/\partial x$ values are different. Although τ_{RW} is a good guideline for WE and EAW when $\partial T/\partial x$ is constant as shown in Figs. 3 and 4, EAW cannot be determined solely by τ_{RW} as shown in Figs. 6 and 7 when $\partial T/\partial x$ changes.

4.2 Linear velocity

Next, we examine the relationship between τ_{RW} and v. Figure 8 shows the dependence of bER on (a) H_w and (b) τ_{RW} for various v values. Open circles also indicate the bER for EAW when τ_{RW} = 0.1 ns. The bER at τ_{RW} = 0.1 ns for v = 20 m/s is higher than that for 10 m/s as shown in Fig. 8 (b). This difference can be explained using Fig. 9. Since Fig. 9 (a) and (b) show the case where v = 10 m/s and 20 m/s, respectively, the τ_{min} values are 0.68 ns and 0.34 ns for Fig. 9 (a) and (b), respectively. The bER for EAW is determined by p_- after τ_{min}. Since the ratios of τ_{RW} to τ_{min} are 14.6 % and 29.3 % for Fig. 9 (a) and (b), respectively, the p_- value after τ_{min} for v = 20 m/s is higher than that for v = 10 m/s. Therefore, the bER for EAW at τ_{RW} = 0.1 ns for v = 20 m/s becomes higher than that for v = 10 m/s. EAW cannot be determined solely by τ_{RW} as shown in Figs. 8 and 9 when v changes.

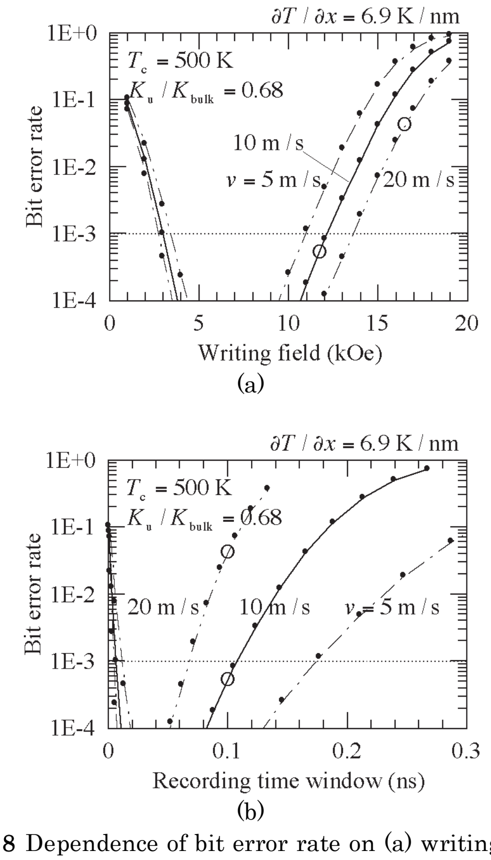

Fig. 8 Dependence of bit error rate on (a) writing field and (b) recording time window for various linear velocities v.

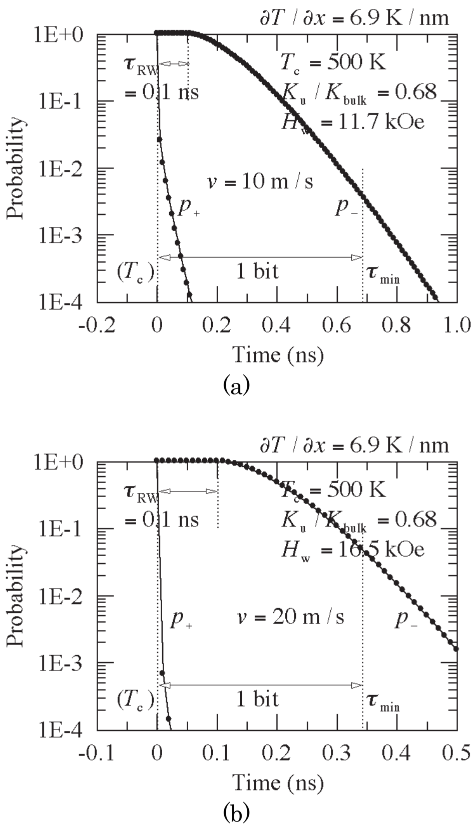

Fig. 9 Dependence of reversal probability of grain magnetization on time for (a) linear velocities v = 10 m/s and (b) 20 m/s.

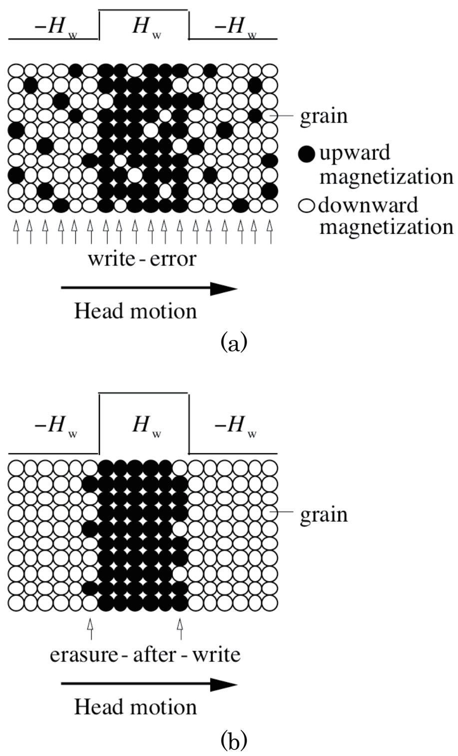

Fig. 10 Schematic illustrations of (a) write-error and (b) erasure-after-write.

Figure 10 shows a schematic illustration of (a) WE and (b) EAW where the bit and the track pitches are much longer than those of this calculation. WE occurs in every grain column during writing as shown in Fig. 10 (a) considering Fig. 4 (a) when H_w is too low. On the other hand, EAW occurs at one or two columns of grains on just the former bit edge as shown in Fig. 10 (b) considering Fig. 4 (b) when H_w is too high. Although WE is independent of bit pitch, the influence of EAW depends on bit pitch, and when the bit pitch is long, it is difficult to examine the influence of EAW. Since the bit pitch is short in this calculation, the influence of EAW can be accurately examined, and EAW will be important for the density of 4 Tbpsi.

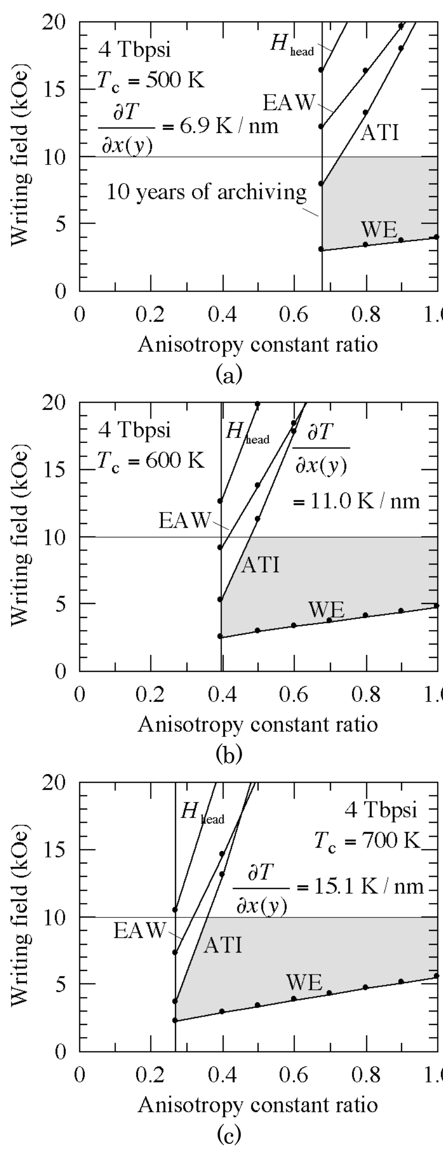

Fig. 11 Allowable range of writing field and anisotropy constant ratio for (a) Curie temperatures T_c = 500 K, (b) 600 K, and (c) 700 K where WE, EAW, ATI, and H_{head} are write-error, erasure-after-write, adjacent-track-interference, and the maximum head field under the main pole, respectively.

4.3 Allowable range

This model calculation can estimate the allowable range of H_w and K_u/K_{bulk}.

In Fig. 11, condition I (10 years of archiving) determines the minimum K_u/K_{bulk} value, and condition II (WE) determines the minimum H_w value. The maximum H_w value is determined from condition III (EAW), condition IV (ATI), and condition V (H_{head}) as mentioned in **3.4**. The maximum H_w value that the writing head can supply was assumed to be 10 kOe. As a result, the gray regions indicate the allowable range. The limiting factors are 10 years of archiving, WE, and ATI in this calculation.

$\partial T/\partial x(y)$ is simultaneously increased as T_c increases in Fig. 11 (a), (b), and (c) as mentioned in **2.3**. The minimum K_u/K_{bulk} value (10 years of archiving) becomes low as T_c increases, and then the allowable range widens as T_c increases.

The reason for the shift of the minimum K_u/K_{bulk} value (10 years of archiving) can be explained using the temperature dependence of K_{um} as shown in Fig. 12 where the K_u/K_{bulk} values are the same. The rates at which K_u increase ($\partial K_u/\partial T$) are almost the same. K_{um} at T_a for T_c = 500 K is insufficient for 10 years of archiving since the temperature difference between T_c and T_a is small. On the other hand, K_{um} at T_a for T_c = 700 K is sufficient. Therefore, the small K_u/K_{bulk} value becomes allowable as T_c increases.

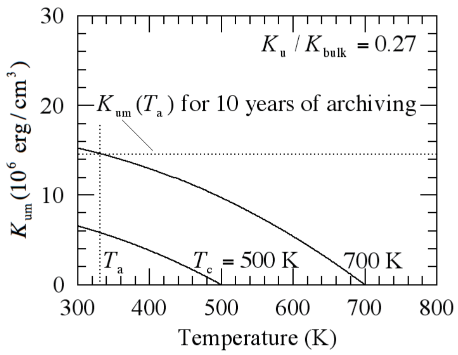

Fig. 12 Dependence of mean anisotropy constant K_{um} on temperature for Curie temperatures T_c = 500 K and 700 K.

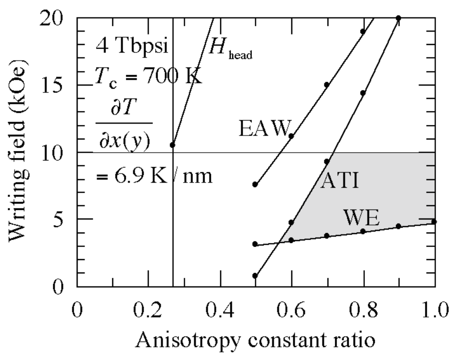

Fig. 13 Allowable range of writing field and anisotropy constant ratio for Curie temperature T_c = 700 K and heat-transfer thermal gradient $\partial T/\partial x(y)$ = 6.9 K/nm.

Another reason for widening the allowable range is the increase in $\partial T/\partial x(y)$, that is, $\partial T/\partial x(y)$ is simultaneously increased as T_c increases as mentioned in **2.3**. Figure 13 shows the allowable range for T_c = 700 K when $\partial T/\partial x(y)$ is 6.9 K/nm instead of 15.1 K/nm (Fig. 11 (c)). The maximum H_w value restricted by EAW and ATI, which are closely related to $\partial T/\partial x(y)$, is greatly decreased from Fig. 11 (c). If $\partial T/\partial x(y)$ is not simultaneously increased, the overall tendency of the allowable range is not greatly changed by increasing T_c when we compare Fig. 11 (a) and Fig. 13.

Figure 14 shows the allowable range calculated using the thermal conductivity of interlayer 1 κ_{IL1} = 0.04 W/(cmK) reported for sputtered MgO film[10] instead of the standard value of 0.5 W/(cmK)[4]. $\partial T/\partial x(y)$ is decreased from 6.9 K/nm (Fig. 11 (a)) to 5.3 K/nm (Fig. 14 (a)) for T_c = 500 K. Then, the allowable range is greatly decreased. Since the allowable range is sensitive to $\partial T/\partial x(y)$, the thermal conductivity is an important design parameter.

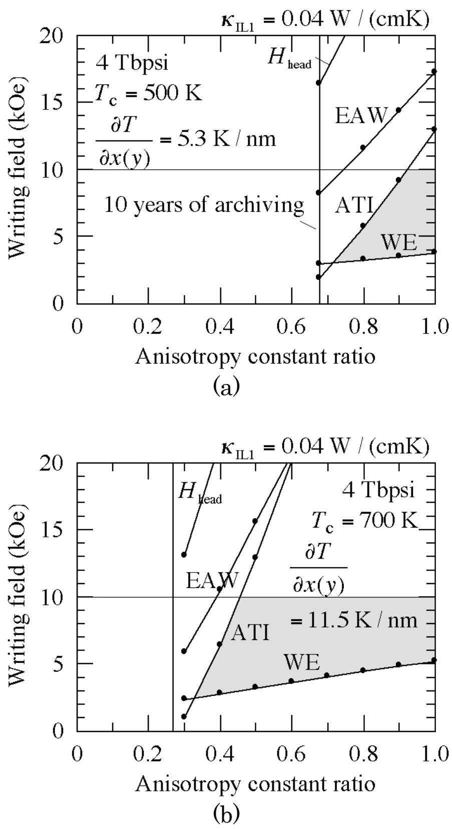

Fig. 14 Allowable range of writing field and anisotropy constant ratio for (a) Curie temperatures T_c = 500 K and (b) 700 K when the thermal conductivity of interlayer 1 κ_{IL1} is 0.04 W/(cmK).

5. Conclusions

We propose a new model calculation using the reversal probability of grain magnetization for heat-assisted magnetic recording. The physical implication of the recording time window τ_{RW}

proposed in the micromagnetic calculation is discussed using a new model calculation. Although τ_{RW} is a good guideline for write-error and erasure-after-write (EAW), EAW cannot be determined solely by τ_{RW}. The influence of EAW is accurately examined, and EAW will be important for the density of 4 Tbpsi.

The allowable range of the writing field and the anisotropy constant ratio K_u / K_{bulk} is also provided for various Curie temperatures T_c. The allowable range widens as T_c increases. The reasons for this are the temperature difference between T_c and the ambient temperature, and the simultaneous increase in the heat-transfer thermal gradient $\partial T / \partial x(y)$ as T_c increases. T_c and $\partial T / \partial x(y)$ are important parameters for reducing K_u / K_{bulk}.

Acknowledgements We acknowledge the support of the Advanced Storage Research Consortium (ASRC), Japan.

References

1) S. H. Charap, P. -L. Lu, and Y. He: *IEEE Trans. Magn.*, **33**, 978 (1997).
2) T. Kobayashi, T. Kitayama, and Y. Fujiwara: *J. Magn. Soc. Jpn.*, **36**, 282 (2012).
3) Y. Isowaki, T. Kobayashi, and Y. Fujiwara: *J. Magn. Soc. Jpn.*, **38**, 1 (2014).
4) T. Kobayashi, Y. Isowaki, and Y. Fujiwara: *J. Magn. Soc. Jpn.*, **39**, 8 (2015).
5) T. Kobayashi, Y. Isowaki, and Y. Fujiwara: *J. Magn. Soc. Jpn.*, **39**, 139 (2015).
6) T. Kobayashi, Y. Isowaki, and Y. Fujiwara: *J. Magn. Soc. Jpn.*, **40**, 1 (2016).
7) T. Kobayashi, Y. Isowaki, and Y. Fujiwara: *J. Magn. Soc. Jpn.*, **40**, 28 (2016).
8) T. Kobayashi and Y. Fujiwara: *J. Magn. Soc. Jpn.*, **40**, 81 (2016).
9) J. -G. Zhu and H. Li: *IEEE Trans. Magn.*, **49**, 765 (2013).
10) S. –M. Lee, D. G. Cahill, and T. H. Allen: *Phys. Rev.* B, **52**, 253 (1995).

Received Mar. 31, 2016; Accepted Nov. 7, 2016

J. Magn. Soc. Jpn., **41**, 10-13 (2017)

<Paper>

Optimum preparation conditions of Fe-deficient Ca-based M-type ferrite

M. Shigemura, K. Watanabe*, K. Kakizaki, and K. Kamishima

Graduate School of Science and Engineering, Saitama University, *255 Shimo-okubo, Sakura-ku, Saitama, Japan*

*Biomolecular Characterization Unit, Center for Sustainable Resource Science, RIKEN, *2-1 Wako, Saitama 351–0198, Japan*

We investigated synthesis conditions and magnetic properties of Fe-deficient Ca-based hexagonal ferrites, $Ca_{1-x}La_xFe_yO_{19-\sigma}$ (x = 0.1–0.3, y = 2.0–10), and found the formation of M-type ferrite at x = 0.1–0.3 and y = 7.0–9.0 above 1200°C. Samples of y = 2.0–6.0 showed deviation from the initial compositions since molten calcium-rich oxide (possibly $CaFe_2O_4$) leaked out from the samples above 1200°C. The X-ray diffraction pattern of $Ca_{0.8}La_{0.2}Fe_{8.0}O_{19-\sigma}$ sintered at 1250°C demonstrates the single phase of M-type hexagonal ferrite. The saturation magnetization of this sample was 68.0 Am^2/kg at room temperature and its Curie temperature was about 400°C, which is slightly lower than that of the Sr-based M-type ferrite (460°C).

Keywords: hexagonal ferrites, M-type, calcium compound

1. Introduction

M-type ferrite is a type of hexagonal ferrite. Its chemical formula is expressed as $M^{2+}Fe^{3+}_{12}O_{19}$ ($M^{2+}=Ba^{2+}$, Sr^{2+}). The M-type ferrite has high saturation magnetization and high coercivity and is mainly used as a permanent magnet. The Curie temperatures of $BaFe_{12}O_{19}$ and $SrFe_{12}O_{19}$ are 450°C and 460°C, respectively.[1)-4)]

The unit cell of M-type ferrite is composed of two kinds of block units, where a R-block and a S-block are stacked up alternately (RSR*S*). The symbol * means 180° rotation of the corresponding block around the c-axis.[1), 3), 4)] The M-type ferrite has ions of $2(MFe_{12}O_{19})$ in the unit cell (RSR*S*), as shown in Fig. 1.

The S-block with the chemical formula of $(2Fe_3O_4)^{2+}$ is identical to the cubic spinel structure. Two close-packed large oxygen anion layers (O layers) build the framework of the S-block. One octahedral (up-spin) and two tetrahedral (down-spin) sites exist for small Fe^{3+} cations in the S-block. [1), 3), 4)]

The R-block contains another kind of close-packed large ion layer with M^{2+}:O^{2-} = 1:3 (M-O layers). The R-block with the chemical formula of $(MFe_6O_{11})^{2-}$ is made up of three large-ion layers where one M-O layer is sandwiched between two O layers. A trigonal-bipyramidal (up-spin) site is just on the M-O layer in the R-block. Two octahedral (down-spin) sites are between the M-O and O layers in the R-block. There are three octahedral (up-spin) sites just on the block border between the S- and R-blocks.[1), 3), 4)]

Because an Fe^{3+} ion has the magnetic moment of 5 μ_B, the total magnetization at zero temperature can be estimated from the numbers of the up and down spins with the assumption of a collinear magnetic structure. Typical M-type ferrite has eight up spins and four down spins as shown in Fig. 1. Hence, the net magnetization per formula unit is (8−4)×(5 μ_B) = 20 μ_B.[1), 4)]

In this study, we investigated the synthesis conditions

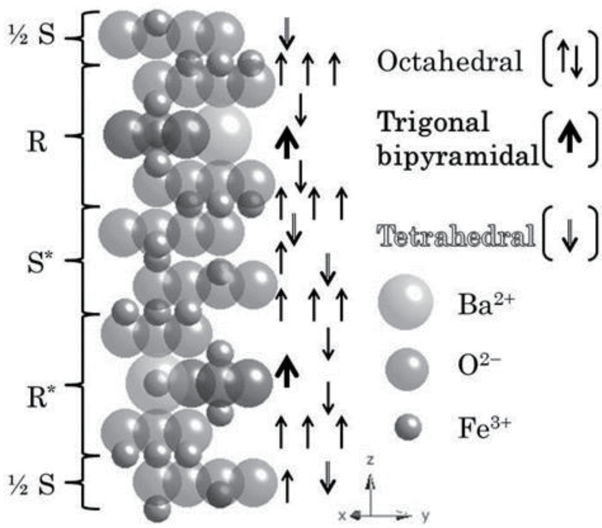

Fig. 1 Spin alignment in the unit cell of the M-type ferrite.

of Ca-based M-type ferrites. Ca is one of the alkaline earth elements. It is attractive to substitute Ca ions for Ba or Sr ions in the hexagonal ferrite because Ca is rich in resouces.[5)] Also, the use of Ca, which is less toxic than Ba, is helpful in terms of producing a safer material.

The synthesis of Ca-based hexagonal ferrites is, however, extremely difficult because the M-type composition sample with Ca:Fe = 1:12 tends to melt and decompose into α-Fe_2O_3, $CaFe_4O_7$, and $CaFe_2O_4$. [6)-8)]

On the other hand, the Ca-based M-type hexaferrite can be synthesized by adding a small amount of La in oxygen atomosphere.[9), 10)] This Ca-based M-type ferrite exists as a ternary oxide of CaO-La_2O_3-Fe_2O_3 because there is no M-type $CaFe_{12}O_{19}$ in the binary CaO-Fe_2O_3 phase diagram as mentioned above. Most of the previous studies, however, treated La_2O_3 as an additive to $CaFe_{12}O_{19}$.[9)-12)] The systematic research was limited at ratio of Fe/(Ca+La)>10 although Fang reported that they obtained the M-type phase by reducing the amount of Fe.[13)] So, the synthesis conditions in air remain unclear. The synthesis condition of the Ca-based M-type ferrite was not systematically surveyed below Fe/(Ca+La) = 9. Therefore, we studied three synthesis conditions: the composition ratio of Ca:La, the ratio of (Ca+La):Fe, and the sintering temperature.

2. Experimental Procedure

Samples of Ca-based M-type ferrite were prepared by a conventional ceramic method. We used $CaCO_3$, La_2O_3, and α-Fe_2O_3 as starting materials. They were mixed in a desired proportion, $Ca_{1-x}La_xFe_yO_{19-\sigma}$ (x = 0.1–0.3, y = 2.0–10). The powder was ball-milled for 24 h. The mixed powder was pressed into a pellet shape and pre-calcined in air at 900°C. The sintered sample was pulverized in a mortar and then milled into fine powder with a planetary ball mill (Fritsch, P-7 Premium line with 1 mmϕ zirconia balls and a 45 ml zirconia container) for 10 min. at 1100 rpm. The processed powder was dried and then pressed into disks. The disks were sintered at 1100 to 1300°C for 5 h. Parts of some sintered samples at $y \leq 6$ were molten above 1250°C. We removed the molten portion adhering to the pellet and employed the remaining part as a sample for measurements. The crystal structure of the sample was examined by powder X-ray diffraction (XRD) analysis with Cu-Kα radiation. The magnetization was measured with a vibrating sample magnetometer (Tamakawa TM-VSM2130HGC) and a superconducting quantum interference device (SQUID) magnetometer (Quantum Design MPMS-XL). The composition was analyzed by the use of an Electron Probe Micro Analyzer (EPMA) (JEOL, JXA-8200). Here, the composition of oxygen was not examined because the analyses of light elements are less accurate than those of heavy elements.

3. Results and discussion

Figure 2 shows the room-temperature saturation magnetization of $Ca_{0.8}La_{0.2}Fe_yO_{19-\sigma}$ (y = 2.0–9.5) sintered at 1200–1300°C. The saturation magnetization was high for the samples sintered above 1250°C with y = 3.0–8.0. However, deviations from the initial compositions seems to take place below y = 6.0 because molten oxides separated out from these initially poor-iron samples, as shown in the inset of Fig. 2. Actually, the EPMA measurement of the sample with the initial composition of y = 4.0 sintered at 1250°C showed the average atomic ratio of Ca:La:Fe = 0.76:0.24:8.53, demonstrating a great deviation from the initial composition. The composition of the molten oxides is possibly close to Ca:Fe = 1:2 because $CaFe_2O_4$ has the lowest melting point of 1216°C in the CaO-Fe_2O_3 system.[6)-8)] The maximum saturation magnetization is 68.0 Am^2/kg for the sample with the

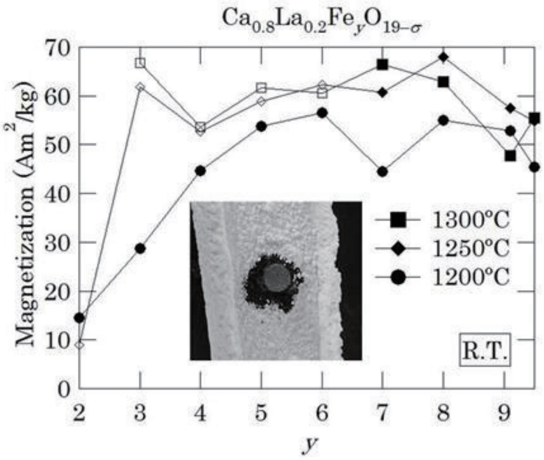

Fig. 2 Saturation magnetization at room temperature of $Ca_{0.8}La_{0.2}Fe_yO_{19-\sigma}$ (y = 2.0–9.5) sintered at 1200, 1250°C and 1300°C. Open markers indicate the samples whose molten portion was removed.

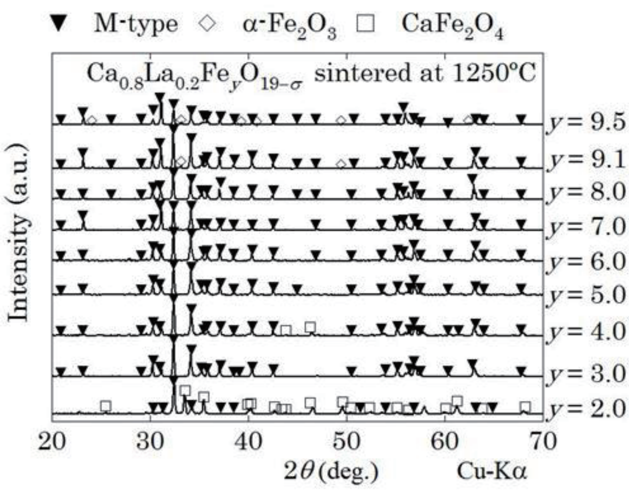

Fig. 3 X-ray diffraction patterns of $Ca_{0.8}La_{0.2}Fe_yO_{19-\sigma}$ (y = 2.0–9.5) sintered at 1250°C.

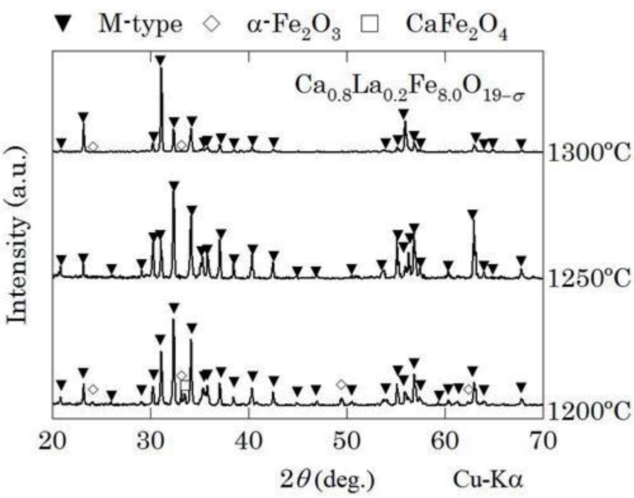

Fig. 4 X-ray diffraction patterns of $Ca_{0.8}La_{0.2}Fe_{8.0}O_{19-\sigma}$ sintered at 1200°C, 1250°C, and 1300°C.

initial composition of Ca:La:Fe = 0.8:0.2:8.0 sintered at 1250°C.

Figure 3 shows the X-ray diffraction patterns of the samples with the initial compositions of Ca:La:Fe = 0.8:0.2:y (y = 2.0–9.5) sintered at 1250°C. The main phase is M-type ferrite for the samples with $y \geq 3.0$.[14), 15)] However, the compositions of the samples with $y \leq 6.0$ are different from the initial compositions because molten calcium-rich oxide (possibly $CaFe_2O_4$) was separated out from the samples sintered at $T \geq 1250$°C. Also, there are minor α-Fe_2O_3 peaks in the X-ray diffraction patterns of the samples with $y \geq 9.1$. Therefore, the initial composition of y = 7.0 or 8.0 is suitable for the preparation of Ca-based M-type ferrite.

Figure 4 shows the X-ray diffraction patterns of $Ca_{0.8}La_{0.2}Fe_{8.0}O_{19-\sigma}$ sintered at 1200°C, 1250°C, and 1300°C. The main phase of these samples is M-type ferrite. However, the sample sintered at 1200°C also has the secondary phases of $CaFe_2O_4$ and α-Fe_2O_3. Since the raw material of α-Fe_2O_3 remains, the sintering temperature of 1200°C is still insufficient for the formation of Ca-based M-type phase. On the other hand, if the sintering temperature was higher than 1300°C, the separation of molten oxides also took place, similar to that shown in the inset of Fig. 2. Therefore, the sintering temperature of about 1250°C is suitable for the preparation of Ca-based M-type ferrite.

Figure 5 shows the X-ray diffraction patterns of $Ca_{1-x}La_xFe_{8.0}O_{19-\sigma}$ (x = 0.1–0.3) sintered at 1250°C. The samples of x = 0.2 and 0.3 have the single phase of M-type ferrite, but the sample of x = 0.1 has the mixed phases of M-type and α-Fe_2O_3. The raw material of α-Fe_2O_3 remains in the Ca-rich sample with $x<0.2$. The lattice constants of these samples are shown in Table 1. The lattice constants of samples are close to those of SrM. On the other hand, the c-axis lattice constants are smaller than that of BaM. This is caused by the difference in the ionic radii because the ionic radii of Ca^{2+}, La^{3+}, Sr^{2+}, and Ba^{2+} are 1.12 Å, 1.16 Å, 1.26 Å, and 1.42 Å, respectively.[16)] The Ba cations with the large ionic radius may expand the c-axis of the BaM ferrite.

Figure 6 shows the temperature dependence of magnetization of $Ca_{1-x}La_xFe_{8.0}O_{19-\sigma}$ (x = 0.1–0.3) sintered at 1250°C. The Curie temperatures of these samples were about 400°C, which is slightly lower than that of the Sr-based M-type ferrite (460°C).[2)]

Table 2 shows the experimental results of the chemical composition analysis of the maximum saturation magnetization sample with the initial composition of Ca:La:Fe = 0.8:0.2:8.0 sintered at 1250°C. The compositions of Ca and La are similar to the initial amounts, but the composition of Fe is slightly larger than the initial amount. Therefore, the M-type ferrite was formed with the composition of $Ca_{0.83}La_{0.17}Fe_{8.9}O_{19-\sigma}$. The difference from the initial composition may be caused by low-melting-point calcium-iron oxides such as $CaFe_2O_4$ that can be eluted off from the M-type grain.

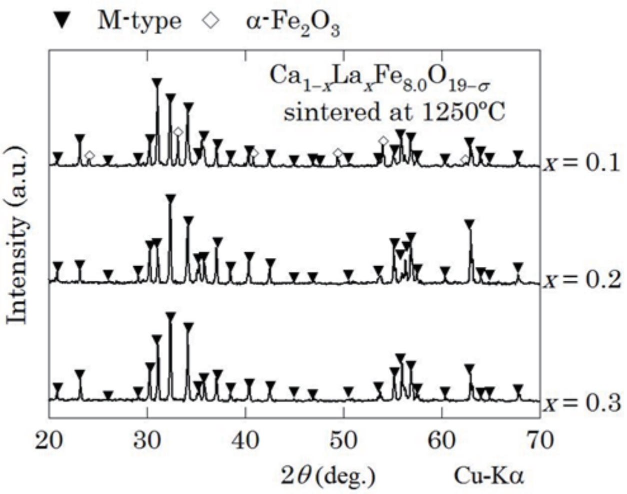

Fig. 5 X-ray diffraction patterns of $Ca_{1-x}La_xFe_{8.0}O_{19-\sigma}$ (x = 0.1–0.3) sintered at 1250°C.

Table 1 Lattice constants of $Ca_{1-x}La_xFe_{8.0}O_{19-\sigma}$ sintered at 1250°C.

		a(Å)	c(Å)
y = 0.8 sintered at 1250°C	x = 0.3	5.892	22.98
	x = 0.2	5.887	23.00
	x = 0.1	5.894	23.03
$SrFe_{12}O_{19}$ (SrM)[14)]		5.884	23.04
$BaFe_{12}O_{19}$ (BaM)[15)]		5.889	23.22

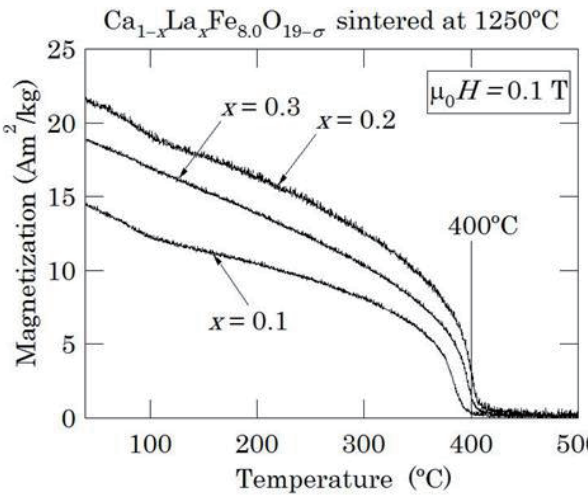

Fig. 6 Temperature dependence of magnetization of $Ca_{1-x}La_xFe_{8.0}O_{19-\sigma}$ (x = 0.1–0.3) sintered at 1250°C.

Figure 7 shows the magnetization curves at 5 K (−268°C) and 300 K (27°C) of $Ca_{0.8}La_{0.2}Fe_{8.0}O_{19-\sigma}$ sintered at 1250°C. The spontaneous magnetization at 5 K (−268°C) is estimated to be 14.7 μ_B/f.u (104 Am^2/kg) by linear extrapolation of the magnetization curve from

Table 2 The result of composition analysis of $Ca_{0.8}La_{0.2}Fe_{8.0}O_{19-\sigma}$ sintered at 1250°C.

Element	Average (at.%)
Ca	8.328
La	1.761
Fe	89.91
Fe/(Ca+La)	8.912

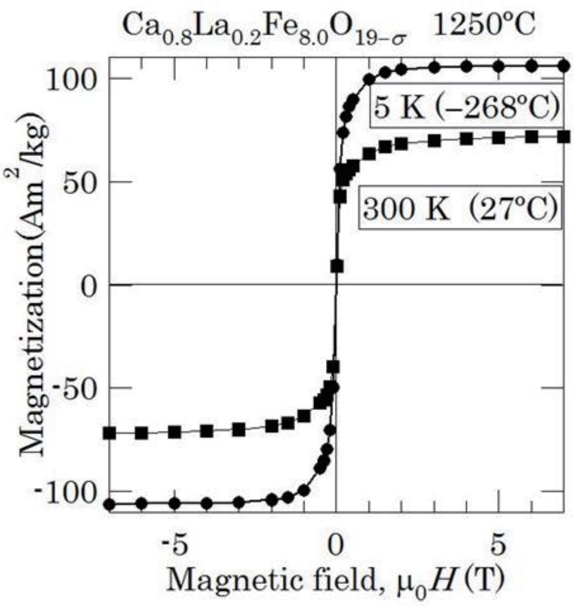

Fig. 7 Magnetization curves at 5 K (−268°C) and 300 K (27°C) of $Ca_{0.8}La_{0.2}Fe_{8.0}O_{19-\sigma}$ sintered at 1250°C.

the high field region of $2 \leq \mu_0 H \leq 7$ T.

We would like to estimate the magnetic moment of the Ca-based hexaferrite. The hexaferrite ($MFe_{12}O_{19}$; M=Ba^{2+}, Sr^{2+}) consists of the R-block ($[MFe_6O_{11}]^{2-}$) and the S-block ($[2Fe_3O_4]^{2+}$), as shown in Fig. 1. The spin arrangements in the R- and S-blocks are similar to each other in spite of the different block structures. There is one central up-spin site between two down-spin sites in each block. There are three up-spin sites between the R-blocks and S-blocks. Therefore, the spin distribution is such that the number of up-spin sites is twice that of the down-spin sites (up:down = 2:1).

The EPMA analysis implied that the chemical formula was approximately $Ca_{0.8}La_{0.2}Fe_{9.0}O_{14.6}$ as shown in Table 2. Here, the composition ratio of oxygen is estimated from the charge balance with the concentration of Ca^{2+}, La^{3+}, and Fe^{3+} cations. In this chemical formula, six of nine spins are in up direction and the other three spins are in down direction with respect to the spin distribution ratio (up:down = 2:1). This estimated magnetic moment of 15 μ_B/f.u. is consistent with the observed magnetization at 5 K (−268°C).

4. Conclusion

We have investigated the synthesis conditions and magnetic properties of Fe-deficient Ca-based M-type ferrite. The sintering temperature of the best sample was 1250°C and the analyzed composition was approximately Ca:La:Fe = 0.8:0.2:9.0. The saturation magnetization of the best sample was 68.0 Am^2/kg at room temperature and 104 Am^2/kg at 5 K (−268°C). The Curie temperature of this sample was about 400°C.

References

1) J. Smit and H. P. J. Wijn: Ferrites, pp. 182–184, pp. 193–194 (Philips Technical Library, Netherlands 1959).
2) S. Chikazumi: Physics of Ferromagnetism, p. 212 (Oxford University Press, Oxford, 2009).
3) G. W. Rathenau: *Rev. Mod. Phys.*, **25**, 297 (1953).
4) Ü. Özgür, Y. Alivov, and H. Morkoc: *J. Mater. Sci-Mater. El.*, **20**, 789 (2009).
5) F. W. Clarke and H. S. Washington: The Composition of the Earth's Crust, pp. 20–21 (United States Geological Survey, Washington, 1924).
6) B. S. Boyanov: *J. Min. Met.,* **41 B**, 67 (2005).
7) M. Hillert, M. Selleby, and B. Sundan: *Metall. Trans. A*, **21A**, 2759 (1990).
8) B. Philips and A. Muan: *J. Am. Ceram. Soc.*, **41**, 445 (1958).
9) N. Ichinose and K. Kurihara: *J. Phys. Soc. Jpn.*, **18**, 1700 (1963).
10) H. Yamamoto, T. Kawaguchi, and M. Kagakura: *IEEE Trans. Magn.*, **15**, 1141 (1979).
11) T. T. Fang, H. B. Lin, and K. T. Lee: *J. Am. Ceram. Soc.*, **71**, C368 (1988).
12) T. T. Fang and K. T. Lee: *J. Am. Ceram. Soc.*, **72**, 2304 (1989).
13) T. T. Fang and J. B. Hwang: *J. Am. Ceram. Soc.*, **75**, 915 (1992).
14) K. Kimura, M. Ohgaki, K. Tanaka, and F. Marumo: *J. Solid State Chem.*, **87**, 186 (1990).
15) The Powder Diffraction File (PDF00-039-1433) by the Internal Center for Diffraction Data (ICDD): W. Wong-Ng, H. McMurdie, B. Paretzkin, C. Hubbard, and A. Dragoo, NBS (USA). ICDD Grant-in-Aid, (1988).
16) R. D. Shannon: *Acta Cryst.* , **A32**, 751 (1976).

Received Jul. 29, 2016; Revised Sept. 27, 2016; Accepted Nov. 7, 2016

J. Magn. Soc. Jpn., **41**, 14-19 (2017)

<Paper>

Study on Electromagnetic Levitation System for Ultrathin Flexible Steel Plate Using Magnetic Field from Horizontal Direction

T. Narita, M. Kida*, T. Suzuki*, and H. Kato
Department of Prime Mover Engineering, Tokai Univ., *4-1-1 Kitakaname, Hiratsuka-shi, Kanagawa 259-1292, Japan*
*Course of Mechanical Engineering, Graduate School of Tokai Univ.

In the transport system of a thin-steel-plate production line, the quality of the plate surface deteriorates over time because of contact with rollers. As a solution to this problem, we have proposed the use of electromagnets to control the horizontal displacement of the steel plate. Vertical force to support the steel plate and horizontal force to suppress elastic vibration are applied to the steel plate by using the horizontal electromagnet. Focusing on these forces, we proposed a magnetic levitation system for the steel plate using only electromagnets installed in the horizontal direction. In this paper, the suspension force in the proposed system is analyzed by the finite element method, and the possibility of applying the proposed system for thinner steel plates is considered. Suspension force is effectively generated owing to the thinness of the steel plate. The results, indicate the proposed magnetic levitation system to be effective for thin steel plates. To verify the validity of the analytical conclusion, an electromagnetic suspension experiment has been carried out, and suspension force generated by the electromagnet has been measured. The agreement between the experimental and analytical results, confirmed the validity of the analytical results.

Key words: electromagnetic levitation, thin steel plate, noncontact support, finite element method

1. Introduction

Thin steel plates are widely used in various industrial products. However, there are the problems of the deterioration of the surface quality and the occurrence of metal plating during transport owing to contact between the steel plate and rollers. As a solution to these problems, a noncontact transport of steel plates using electromagnetic force has been proposed [1)-4)]. However, in these considerations, electromagnets are installed in the vertical direction. In this method, if the steel plate is thin and does not have sufficient flexural rigidity, it is difficult to add suspension force for levitation over the entire steel plate. Previously, the electromagnetic levitation system for steel plates had electromagnets installed in the horizontal direction as well as the vertical direction. This system is able to transport a magnetically levitated steel plate [5)]. Moreover, a similar experiment for an ultrathin steel plate was performed, and the noncontact transport of ultrathin steel plates was demonstrated [6)-7)]. However, since this proposed system requires a number of control channels, there are the problems of complexity and high cost.

Because of the magnetic field of the added electromagnets, attractive force acts in the steel plate as the vertical suspension force as well as the horizontal tension force. The tension force can add the suspension force to the entire steel plate, and it becomes possible to improve the levitation stability. Moreover, the tension can prevent the plastic deformation of the steel plate, such as dimpling and folding. This can be expected to lead to surface quality improvement of the steel plate. Focusing on these forces, the feasibility of a magnetic levitation system for steel plates using only electromagnets installed in the horizontal direction was considered. Electromagnetic field analysis by the finite element method (FEM) was performed, and we confirmed that the proposed system could levitate a steel plate with a thickness of 0.3 mm [8)]. However, these results have not been verified experimentally. Furthermore, the effectiveness of this system for thinner steel plates has not been considered. In this study, the suspension force in the proposed system is analyzed by the FEM and the applicability of the proposed system to thinner steel plates is considered. In addition, electromagnetic suspension experiments are performed with the steel plate thickness of 0.30 mm or 0.24 mm. To show the effectiveness of this system for thinner steel plates, analytical and experimental results are discussed in detail.

2. FEM analyses of suspension force of electromagnet

Figure 1 shows an outline of the proposed system. A zinc-coated steel plate is levitated and positioned in the noncontact mode by the attractive forces of electromagnets that are controlled on the basis of feedback signals from laser sensors.

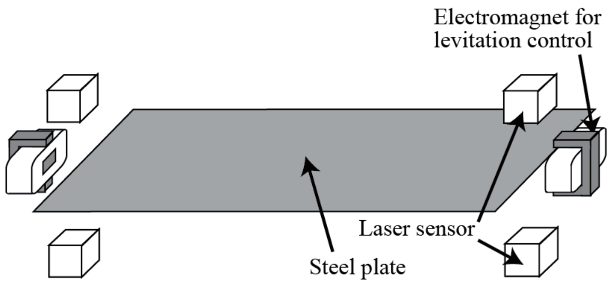

Fig. 1 Electromagnetic levitation system for steel plate using only electromagnets installed in horizontal direction.

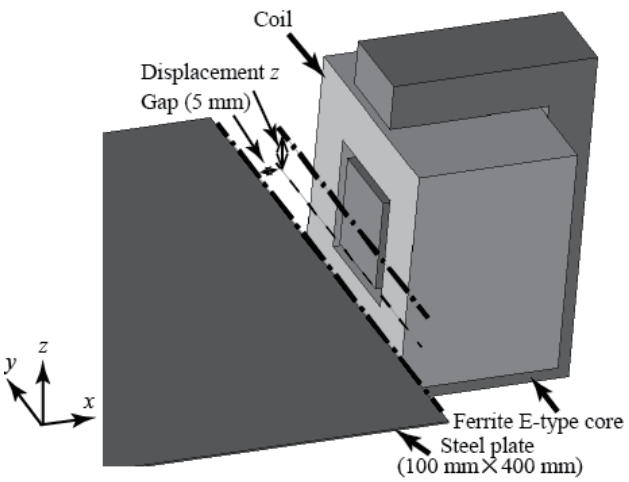

Fig. 2 FE analytical model.

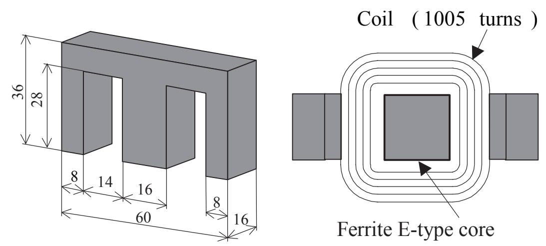

Fig. 3 Schematic illustration of electromagnet.

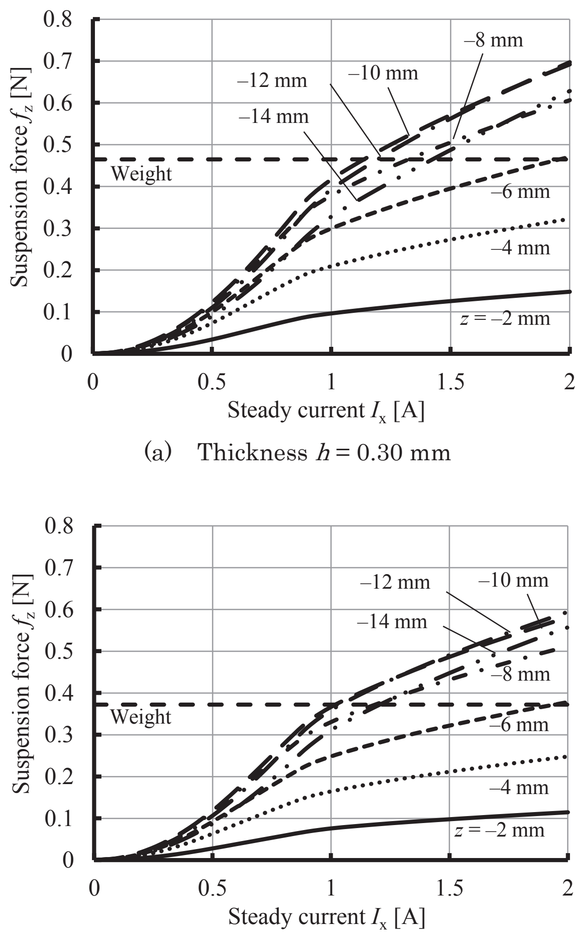

(a) Thickness h = 0.30 mm

(b) Thickness h = 0.24 mm

Fig. 4 Relationship between thickness of steel plate h and vertical attractive force f_z for each displacement z.

In the previous study[7], it has been confirmed that this control system can control horizontal displacement of the steel plate (length 400 mm, width 100 mm, thickness 0.18 mm, material SS400 steel), and suppress the standard deviation of horizontal displacement less than 0.1 mm. From the above, it was confirmed that the proposed system has a practically sufficient control performance for positioning control in the horizontal direction.

2.1 FE model and analytical conditions

To discuss the effectiveness of this system, suspension force is analyzed by the FEM. The electromagnetic field analysis is carried out using the finite-element method software JMAG (Ver. 11). The analytical model is shown in Fig. 2. The steel plate (length 400 mm, width 100 mm, material SS400 steel) is levitated with electromagnets shown in Fig. 3. In previous studies[8], analytical results showed that this electromagnet can generate a sufficient horizontal tension for positioning control more than 2 times greater than vertical suspension force. Furthermore, it has been confirmed that the steel plate is hardly displaced in the control direction with horizontal positioning control[7]. Therefore, the analysis is carried out on the assumption that the steel plate does not displaced from the control point.

The analytical conditions are as follows. Vertical displacement z is changed from −2 mm to −14 mm. The gap between the edge of the steel plate and the surface of electromagnets is 5 mm. The steady electromagnet current I_x is in the range from 0.1 A to 2.0 A. The thickness of the steel plate h is changed from 0.06 mm to 0.30 mm with each increase in thickness of 0.06 mm.

2.2 Numerical results by FEM

Figure 4 shows the relationship between steady current I_x [A] and vertical suspension force f_z [N]. Figure 4(a) shows the analytical result for the steel plate with a thickness of 0.30 mm. Figure 4(b) shows the result for a plate thickness of 0.24 mm. Dotted lines in these figures mean the weight of the steel plate. If the generated suspension force is equal to the weight of the steel plate, the steel plate can be levitated. Analytical results show that increasing the steady current leads to upward displacement of the steel plate. When the steady current is greater than 1.0 A, the suspension force is increased gradually, because magnetic saturation occurs in the core. When the steel plate is displaced downward, suspension force increases. The results in Fig 4(a) indicate that the steel plate can be levitated when displacement is greater than −6 mm. However, even if the steel plate is displaced more than −10 mm, suspension force does not increase further. The cause of this result is the magnetic field generated from the convex portion of the lower part of the electromagnet core. Although suspension force

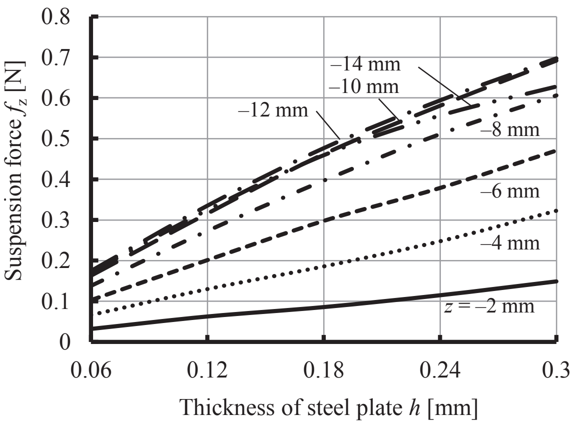

Fig. 5 Relationship between thickness of steel plate h and suspension force f_z for each displacement z (steady current I_x = 2.0 A).

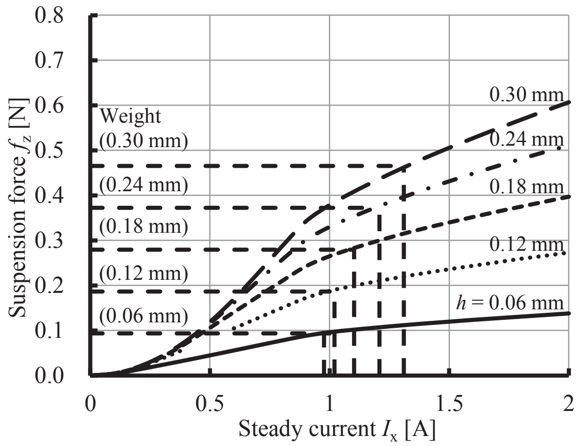

Fig. 7 Relationship between steady current I_x and suspension force f_z for each thickness of steel plate h (displacement z = –8 mm).

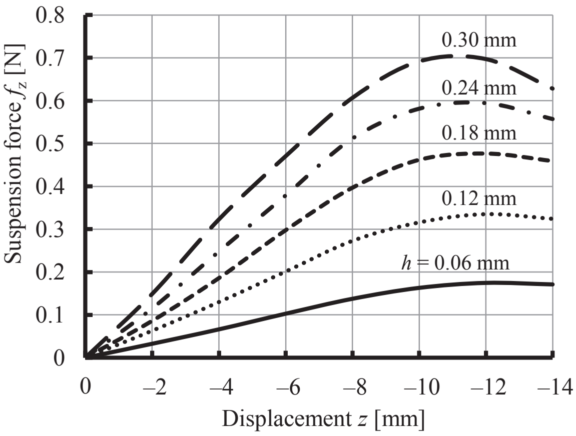

Fig. 6 Relationship between displacement z and suspension force f_z for each thickness of steel plate h (steady current I_x = 2.0 A).

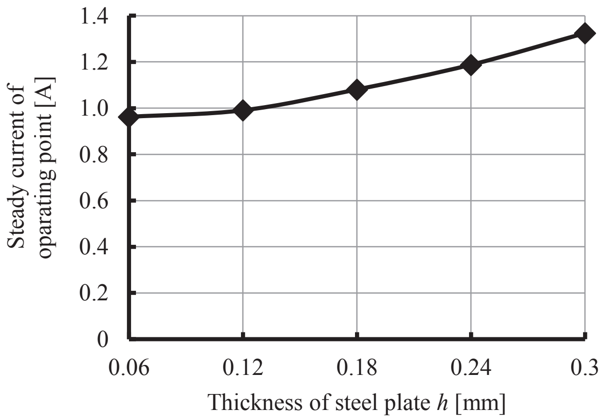

Fig. 8 Relationship between thickness of steel plate h and steady current of operating point (displacement z = –8 mm).

generally decreases, the result for the plate with 0.24 mm thickness shows the same tendency as that for the plate with 0.30 mm thickness, as shown in Fig. 4(b).

Figure 5 shows the relationship between plate thickness and suspension force for each displacement when the steady current is 2.0 A at maximum. The suspension force is reduced in proportion to the decrease in the thickness. The reason for this is considered that the part for generating suspension force becomes smaller when the thickness of steel plate is thinner. Figure 6 shows the relationship between suspension force and displacement for each thickness when the steady current is 2.0 A. The suspension force is linearly proportional to the displacement when the displacement is less than -8 mm. In this linear range, even if the steel plate is vertically displaced by a disturbance, the suspension force acts as a restoring force. With this restoring force, the steel plate stabilizes passively.

Figure 7 shows the relationship between steady current and suspension force for each thickness of steel plate with z = –8 mm. The dotted lines indicate the weight of the steel plate for each thickness. At the operating point where suspension force is equal to its own weight, the steel plate can be levitated. As the steel plate becomes lighter when it becomes thinner, it seems to be more easily levitated. On the other hand, the suspension force is also decreased. From these analytical result, it is found that the decrease in the suspension force is smaller than the decrease in the weight of the steel plate. These results show that decreasing the thickness of the steel plate can reduce the steady current of the operating point. The relationship between the thickness of the steel plate and the steady current of the operating point is shown in Fig. 8. Compared with the result for the thickness of 0.30 mm, the steady current of the operating point is reduced 18.4% in the case of the 0.18 mm thickness, and 27.3% in the case of the 0.06 mm thickness. Suspension force is more effectively generated with increasing thinness of the steel plate. The proposed magnetic levitation system is superior for thin steel plates that are difficult to levitate by the conventional method.

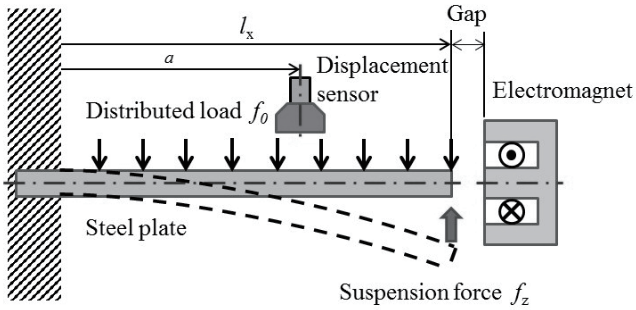

Fig. 9 Experimental model of electromagnetic suspension force.

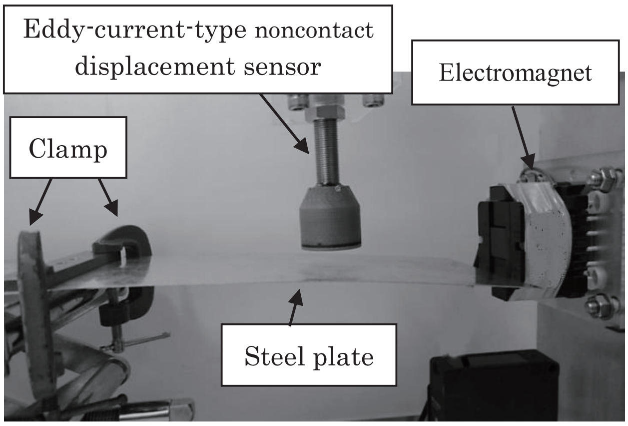

Fig. 10 Photograph of experimental apparatus for electromagnetic suspension.

3. Electromagnetic suspension experiment

3.1 Experimental model

To verify the validity of the above analytical results, the electromagnetic suspension experiment is carried out. Experimental model is shown in Fig. 9. An electromagnet is installed near the end of the fixed steel plate. An eddy-current-type noncontact displacement sensor is installed above the steel plate to measure the displacement of the steel plate. Distributed and concentrated loads act on the steel plate. Distributed load is due to its own weight, and concentrated load is due to suspension force by from the electromagnet.

Vertical displacement z' [m] of the steel plate without suspension force f_z [N] from the electromagnet and vertical displacement z [m] with f_z are expressed as [9]

$$z'(x)=\frac{f_0}{EI}\left(\frac{1}{24}x^4-\frac{l_x}{6}x^3+\frac{l_x^{\,2}}{4}x^2\right) \quad (1)$$

$$z(x)=z'(x)+\frac{f_z}{EI}\left(-\frac{1}{6}x^3+\frac{l_x}{2}x^2\right). \quad (2)$$

Distributed load f_0 [N/m] due to self-weight is expressed as

$$f_0=\rho g h l_y \ , \quad (3)$$

where x is the horizontal displacement [m], l_x the length of the steel plate [m], l_y the width of the steel plate [m], h the thickness of steel plate [m], ρ the plate density [kg/m³], g the acceleration due to gravity [m/s²], E Young's modulus of the thin steel plate [N/m²], I the second moment of area [m⁴], and a the sensor position from the fixed end [m].

Suspension force f_z is obtained by measuring displacements z and z' at sensor position a, as

$$f_z=\frac{EI}{-\frac{1}{6}a^3+\frac{l_x}{2}a^2}\left(z(a)-z'(a)\right) \quad (4)$$

Table 1 Parameters and values.

Parameter	Value
ρ	7500 kg/m³
l_x	0.20 m
l_y	0.10 m
h	0.30×10⁻³ m, 0.24×10⁻³ m
a	0.115 m
E	206 GPa
g	9.81 m/s²

3.2 Experimental conditions

Table 1 shows the specifications of the experiment. Figure 10 is the photograph of the experimental apparatus for electromagnetic suspension. The steel plate is fixed with clamps. In the vertical direction, the electromagnet is installed at the same position as the supporting position. The gap between the surface of the electromagnet and the edge of the steel plate end is 5 mm. Vertical displacement of the steel plate is measured with a sensor when the steady current of the electromagnet is changed from 0 A to 2.0 A. In this experiment, the edge of the steel plate tilts about 5° due to deflection. This experimental condition is different from analytical condition in chapter 2. However, the attractive force generates locally at the only edge of steel plate[8]. Furthermore, we analyzed previously the attractive force generated at steel plate when the steel plate tilts 5°. Comparing analytical result of tilt angle 0° and 5°, amount of change of the suspension force f_z was less than 5%. Therefore, it is confirmed that the deflection of the steel plate does not affect suspension force.

3.3 Experimental results

Figure 11 shows the relationship between steady current and displacement. Figure 11 (a) shows the result for the plate with 0.30 mm thickness. Figure 11 (b) shows the result for the plate with 0.24 mm thickness. Previously, the experimental value measured with a sensor was compared with the calculated value with the steady current of 0 A. The result has confirmed that the differences between experimental and calculated values

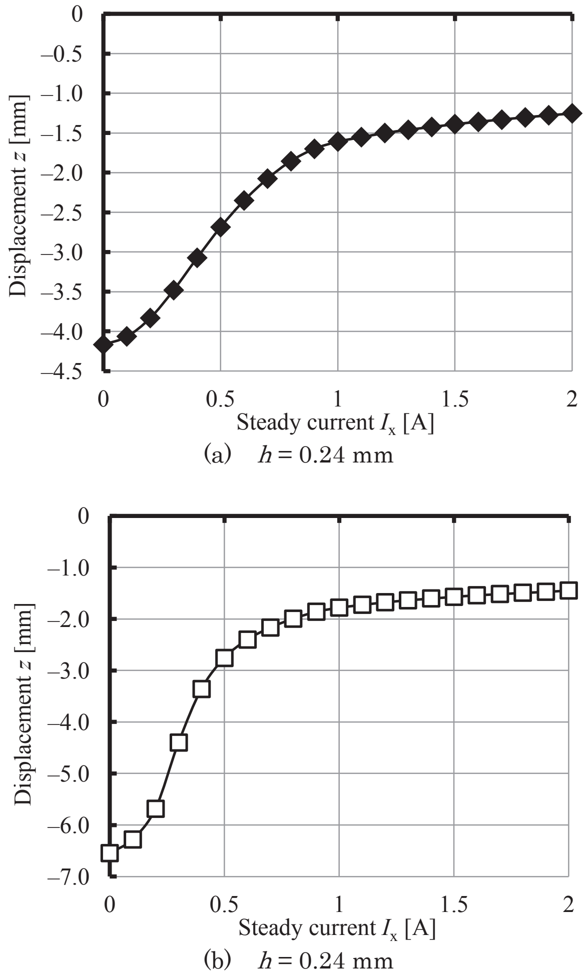

Fig. 11 Relationship between steady current I_x and measured displacement z by sensor.

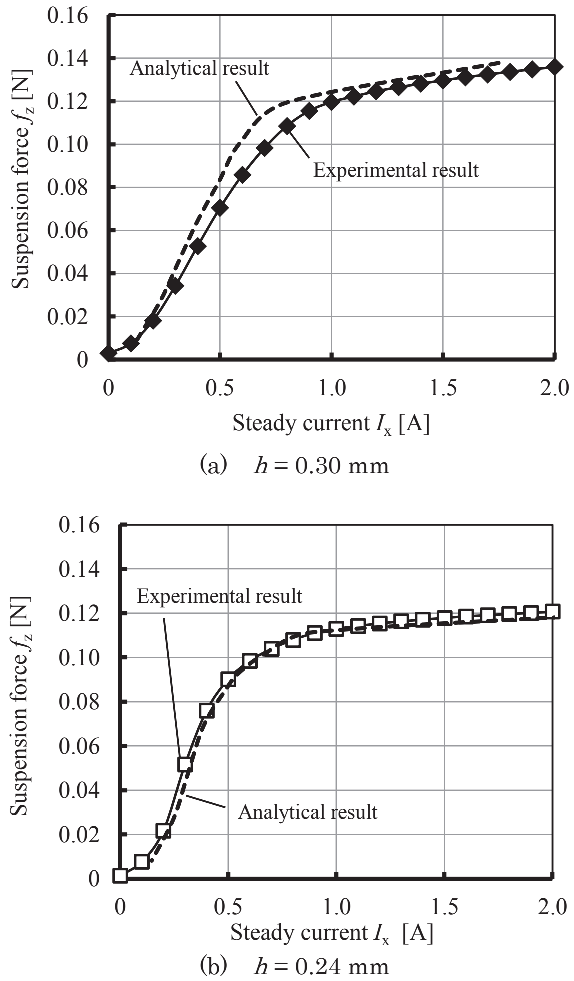

Fig. 12 Relationship between steady current I_x and calculated suspension force f_z for measured displacement and analytical results

are less than 1%. Experimental results show that increasing the steady current leads to upward displacement of the steel plate. This trend is significant when the steady current is less than 0.5 A.

Figure 12 shows the relationship between steady current and suspension force calculated using the experimental result. Figure 12 (a) shows the result for the plate with 0.30 mm thickness. Figure 12 (b) shows the result for the plate with 0.24 mm thickness. The plotted point in this figures indicate experimental results. Suspension force increases with increasing steady current. When the steady current is less than 0.5 A, the increment of suspension force is larger. The attractive force of the electromagnet is generated at the steel plate toward the center of the electromagnet core. If the steel plate is displaced further downward, the ratio of suspension force to attractive force is larger. On the other hand, when the steel plate is displaced upward, the ratio of tension to attractive force is larger. It is considered that the cause of saturation is upward displacement of the steel plate.

Dashed line in Fig. 12 indicates analytical results of suspension force. This analytical suspension force is calculated using eq. (2) when the displacement of the edge of steel plate coincides analysis condition in chapter 2. The analytical steady current is obtained using Fig. 4 when the displacement and analytical suspension force coincides analysis condition.

The experimental results agree the analytical results. In the range of size in this paper, deflection of the steel plate was experimentally confirmed that seldom effect on the suspension force. Furthermore, the agreement of the analytical and experimental results shows the validity of the realization of the magnetic levitation system only using electromagnets in the horizontal direction described in the previous section.

4. Conclusion

In our proposed system using only electromagnets installed in the horizontal direction, vertical suspension force, which was applied to the steel plate by an electromagnet, was analyzed for a steel plate thickness of less than 0.30 mm. In the range of interest in this study, suspension force is more effectively generated as the steel plate becomes thinner. The results indicate the proposed magnetic levitation system to be superior for thin steel plates. To verify the validity of the analytical conclusion, an electromagnetic suspension experiment was carried out using an experimental apparatus for electromagnetic suspension, and suspension force of the electromagnet was measured. The agreement between the experimental and analytical results showed the validity of the analysis.

In the next stage, in order to realize a magnetic levitation system for noncontact transport and suspension of steel plates, a system with improved stability will be designed by installing more electromagnets.

Acknowledgements This work was supported by JSPS KAKENHI Grant Number 15K18010 as the Grant-in-Aid for Young Scientists (B).

References

1) K. Sato, S. Torii: *Trans. IEEJ*, **128,** 267 (2008) , [in Japanese].
2) Y. Kuruma, A. Yamamoto, T. Higuch: 2012 Jpn. Soc. Prec. Eng. Autumn Conf., Kitakyushu, *Jpn. Soc. Prec. Eng.,* 649 (2012), [in Japanese].
3) F. Sun, K. Oka: *Trans. Jpn. Soc. Mech. Eng. Ser. C*, **78**, 2771 (2012), [in Japanese].
4) T. Mizuno, D. Sekine, M. Takasaki, Y. Ishino: *Trans. Jpn. Soc. Mech. Eng.,* **80**, DR0163 (2014), [in Japanese].
5) Y. Oshinoya, T. Shimogo: *Proc. Int. Conf. Adv. Mech.,* 845 (1989).
6) S. Akiyoshi, T. Saito, T. Iwata, U. Matrika, Y. Oshinoya, K. Ishibashi, H. Kasuya: *Proc. Int. Council Elec. Eng. 2008 OKINAWA*, P-068 (2008).
7) T. Narita, Y. Oshinoya, and S. Hasegawa: *Jour. Int Council Elec. Eng.*, **1**, 292 (2011).
8) T. Narita, Y. Ootsuka, M. Ooshima, H. Kato, Y. Oshinoya:, Proc. 23rd MAGDA Conf., Takamatsu, *Jpn. Soc. Appl. Elec. Mech.,* 123 (2014), [in Japanese].
9) K. Oonishi: JIS ni Motoduku Kikaisekkeiseizu Binran (in Japanese), 12th ed., p. 4-8 (Ohmsya, Tokyo, 2015)

Received May 13, 2016; Revised July. 7, 2016; Accepted Nov. 18, 2016

Journal of the Magnetics Society of Japan

Vol. 41 No. 1 (通巻第289号) 2017年1月1日発行

Vol. 41 No. 1 Published Jan 1, 2017
by the Magnetics Society of Japan
Tokyo YWCA building Rm207, 1–8–11 Kanda surugadai, Chiyoda-ku, Tokyo 101–0062
Tel. +81–3–5281–0106 Fax. +81–3–5281–0107

Printed by JP Corporation Co., Ltd.
2–3–36, Minamikase, Saiwai-ku, Kanagawa 212–0055
Advertising agency: Kagaku Gijutsu-sha

発行：(公社)日本磁気学会　101–0062 東京都千代田区神田駿河台 1–8–11　東京YWCA会館 207 号室
製本：(株)ジェイピーコーポレーション　212–0055 神奈川県川崎市幸区南加瀬 2–3–36　Tel.（044）571–5815
広告取扱い：科学技術社　111–0052 東京都台東区柳橋 2–10–8　武田ビル4F　Tel.（03）5809–1132